Inflammatory response in hematopoietic stem and progenitor cells triggered by activating SHP2 mutations evokes blood defects

Maja Solman[1], Sasja Blokzijl-Franke[1,*], Florian Piques[2,3,*], Chuan Yan[4,5,6,7], Qiqi Yang[4,5,6,7], Marion Strullu[2,8], Sarah M. Kamel[1], Pakize Ak[1], Jeroen Bakkers[1,9], David M. Langenau[4,5,6,7], Hélène Cavé[2,3], Jeroen den Hertog[1,10,#]

[1] Hubrecht Institute-KNAW and UMC Utrecht, 3584 CT Utrecht, the Netherlands

[2] INSERM UMR_S1131, Institut de Recherche Saint-Louis, University of Paris, Paris, France

[3] Assistance Publique des Hôpitaux de Paris AP-HP, Hôpital Robert Debré, Département de Génétique, Paris, France

[4] Molecular Pathology Unit, Massachusetts General Hospital Research Institute, Charlestown, MA 02129, United States of America

[5] Massachusetts General Hospital Cancer Center, Charlestown, MA 02129, United States of America

[6] Center for Regenerative Medicine, Massachusetts General Hospital, Boston, MA 02114, United States of America

[7] Harvard Stem Cell Institute, Cambridge, MA 02139, United States of America

[8] Assistance Publique des Hôpitaux de Paris AP-HP, Hôpital Robert Debré, Service d'Onco-Hématologie Pédiatrique, Paris, France

[9]Department of Medical Physiology, Division of Heart and Lungs, UMC Utrecht, 3584 CX Utrecht, the Netherlands

[10] Institute of Biology Leiden, Leiden University, 2333 BE Leiden, The Netherlands

* These authors contributed equally

Jeroen den Hertog, **Address**: Hubrecht Institute-KNAW and UMC Utrecht, 3584 CT Utrecht, the Netherlands, **Telephone**: +31 30 212 1800, **Email:** j.denhertog@hubrecht.eu

Abstract

Gain-of-function mutations in the protein-tyrosine phosphatase SHP2 are the most frequently occurring mutations in sporadic juvenile myelomonocytic leukemia (JMML) and JMML-like myeloproliferative neoplasm (MPN) associated with Noonan syndrome (NS). Hematopoietic stem and progenitor cells (HSPCs) are the disease propagating cells of JMML. Here, we explored transcriptomes of HSPCs with Shp2 mutations derived from JMML patients and a novel NS zebrafish model. In addition to major NS traits, CRISPR/Cas9 knock-in Shp2^{D61G} mutant zebrafish recapitulated a JMML-like MPN phenotype, including myeloid lineage hyperproliferation, *ex vivo* growth of myeloid colonies and *in vivo* transplantability of HSPCs. Single cell mRNA sequencing of HSPCs from Shp2^{D61G} zebrafish embryos and bulk sequencing of HSPCs from JMML patients revealed an overlapping inflammatory gene expression pattern. Strikingly, an anti-inflammatory agent rescued JMML-like MPN in Shp2^{D61G} zebrafish embryos. Our results indicate that a common inflammatory response was triggered in the HSPCs from sporadic JMML patients and syndromic NS zebrafish, which potentiated MPN and may represent a future target for JMML therapies.

Introduction

A broad spectrum of heterozygous germline activating mutations in the tyrosine phosphatase SHP2, encoded by *PTPN11* has been found to cause Noonan syndrome (NS), a dominantly inherited developmental disorder from the RASopathy group affecting 1:1,500 individuals. NS is characterized by a systemic impact on development, most commonly resulting in short stature, congenital heart defects and specific craniofacial characteristics (Rauen, 2013; Tajan et al., 2018). Somatic activating mutations in *PTPN11* are the most common cause of sporadic juvenile myelomonocytic leukemia (JMML), a rare but aggressive myelodysplastic and myeloproliferative neoplasm (MPN) occurring in young children (Caye et al., 2015; Tartaglia et al., 2003). Consistently, children with NS are predisposed to developing neonatal MPN, that either regresses without treatment or rapidly progresses to JMML leading to early death (Kratz et al., 2005; Strullu et al., 2014). Previous studies support the view of a strong endogenous role of germline *PTPN11* mutations in the occurrence of myeloproliferative complications with the existence of high-risk mutations (Mulero-Navarro et al., 2015; Strullu et al., 2014). Given the aggressive nature of JMML and lack of therapies, a better understanding of the elusive JMML(-like MPN) pathophysiology and development of reliable preclinical models are essential.

Several lines of evidence indicate the importance of prenatal hematopoiesis such as the young age window for both NS-associated and sporadic JMML. The prenatal origin of *PTPN11* mutations in sporadic JMML suggests that JMML and NS-associated JMML-like MPN originate from fetal hematopoiesis (Behnert et al., 2021). Studying SHP2-driven JMML(-like MPN) during fetal hematopoiesis is challenging in conditional knock-in mouse models of JMML with *PTPN11* mutations, because mutant SHP2 expression is induced only postnatally (Chan et al., 2009; Xu et al., 2011) or indolent MPN is induced (Tarnawsky et al., 2017, 2018). NS knock-in mice with activating *PTPN11* mutations develop mild MPN only after 5 months of age (Araki et al., 2004, 2009).

Zebrafish (*Danio rerio*) with rapid *ex-utero* development, transparent embryos and conserved blood ontogeny emerged as a unique pediatric leukemia model that enables monitoring of leukemogenesis from its initial stages with high temporal and spatial resolution (de Pater & Trompouki, 2018; Gore et al., 2018). Furthermore, NS-associated features, such as shorter body axis length, craniofacial defects, defective

77 gastrulation and impaired heart looping, are recapitulated in zebrafish embryos upon
78 transient over-expression of NS-associated protein variants (Bonetti et al., 2014;
79 Jopling et al., 2007; Niihori et al., 2019; Paardekooper Overman et al., 2014;
80 Runtuwene et al., 2011).

81 To better assess the link between dysregulated SHP2 and myeloproliferation in
82 the context of NS, we developed and characterized a novel genetic zebrafish model
83 of NS with Shp2-D61G mutation, a dominantly inherited NS-associated mutation that
84 is most frequently associated with NS/JMML-like MPN in human patients (Strullu et
85 al., 2014; Tartaglia et al., 2001). Mutant zebrafish developed hematopoietic defects
86 consistent with JMML-like MPN. Transcriptomic comparison of HSPCs obtained from
87 JMML patients with somatic *PTPN11* mutations and HSPCs from mutant zebrafish
88 harboring an NS-associated variant of Shp2, suggested common mechanisms of
89 disease initiation in sporadic and syndromic PTPN11-driven JMML. Both data sets
90 show a similar pro-inflammatory gene expression and an anti-inflammatory agent
91 largely rescued the hematopoietic defects in mutant zebrafish, suggesting
92 inflammation as potential drug target for sporadic and syndromic JMML(-like MPN).
93 Our data show that Shp2-mutant zebrafish convincingly model the human NS-
94 associated MPN thereby providing a valuable preclinical model for development of
95 future therapies.

96 # Results

97 **Shp2^{D61G} mutant zebrafish display typical Noonan syndrome traits**

98 To investigate early hematopoietic defects associated with NS in a vertebrate
99 animal model, we turned to zebrafish, which represents a versatile model to study
100 leukemogenesis and in which it is feasible to introduce mutations at will using
101 CRISPR/Cas9-mediated homology directed repair (Tessadori et al., 2018). NS is a
102 dominant autosomal disorder and 50% of NS patients carry heterozygous mutations
103 in the protein-tyrosine phosphatase SHP2 (*PTPN11*). The zebrafish genome
104 contains two *ptpn11* genes (*ptpn11a* and *ptpn11b*), encoding Shp2a and Shp2b.
105 Shp2a is indispensable during zebrafish development, whereas loss of Shp2b
106 function does not affect development (Bonetti et al., 2014). Certain NS mutations are
107 more frequently associated with NS/JMML-like MPN than others. The D61G
108 substitution in SHP2 is the most frequently occurring (Strullu et al., 2014; Tartaglia et
109 al., 2001). The homology between human SHP2 and zebrafish Shp2a is 91% and
110 the amino acid D61 is located in an absolutely conserved region of the protein
111 (**Figure 1-figure supplement 1A**). Thus, we introduced the D61G mutation in
112 zebrafish Shp2a using CRISPR/Cas9-mediated homology directed repair (**Figure 1-**
113 **figure supplement 1B**), targeting the *ptpn11a* gene. Sequencing confirmed that the
114 oligonucleotide used for the homology directed repair was incorporated correctly into
115 the genome (**Figure 1A**) and that the introduced mutation did not have a detectable
116 effect on Shp2a protein expression (**Figure 1B**). Prior to phenotypic analyses, the
117 mutant lines were outcrossed twice to ensure that potential background mutations
118 due to the CRISPR/Cas9 approach were removed.

119 Genotypically, heterozygous Shp2$^{D61G/wt}$ zebrafish mutants correspond to NS
120 patients. Consistently, in 32% of heterozygous Shp2$^{D61G/wt}$ and 45% of homozygous

121 Shp2$^{D61G/D61G}$ embryos at 5 days post fertilization (dpf) we observed typical Noonan
122 syndrome traits, such as reduced body axis extension, heart edema and craniofacial
123 deformities. Based on the extent of the phenotypes, defects were categorized as
124 normal, mild and severe. (**Figure 1C,D**). The observed phenotypic defects were
125 mostly mild, but in some cases severe defects were found, including severely
126 stunted growth, edemas of the heart and jaw, and absence of the swim bladder
127 (**Figure 1C,D**). A more detailed characterization of the typical NS traits showed that
128 the body axis length was significantly reduced in Shp2^{D61G} mutant embryos at 5dpf
129 (**Figure 1E**). Furthermore, imaging of Alcian blue stained cartilage revealed NS-
130 reminiscent craniofacial defects in 4dpf Shp2^{D61G} mutant embryos, characterized by
131 broadening of the head (**Figure 1F**), leading to an increased ratio of the width of the
132 ceratohyal and the distance to Meckel's cartilage (**Figure 1G**). We also assessed the
133 general morphology and function of the mutant embryonic hearts. Whole-mount *in*
134 *situ* hybridization (WISH) with cardiomyocyte (*myl7*), ventricular (*vhmc*) and atrial
135 (*ahmc*) markers identified no obvious morphological heart defects, such as changes
136 in heart size or heart looping, as well as heart chamber specification at 3dpf (**Figure**
137 **1-figure supplement 1C**). A decrease in heart rate (**Figure 1I)**, ejection fraction and
138 cardiac output (**Figure 1-figure supplement 1D,E**) was detected from the
139 ventricular kymographs obtained from high speed video recordings (Tessadori et al.,
140 2012) of the Shp2^{D61G} mutant hearts at 5dpf **(Figure 1H**). Effects on cardiac function
141 varied from embryo to embryo, which is reminiscent of variable heart defects in
142 human patients.

143 The embryos with severe phenotypic defects did not develop a swim bladder
144 and they did not survive to adulthood. The rest of both Shp2$^{D61G/wt}$ and Shp2$^{D61G/D61G}$
145 mutant zebrafish grew up normally, their life span was not affected, and they

146 displayed rather mild defects in adult stages, such as shorter body axis (**Figure 1J**),
147 with markedly reduced length observed from the embryonic stage of 5dpf until the
148 fully developed adults (**Figure 1K**). In 10% of Shp2^{D61G} mutants the phenotypes
149 were more severe, with markedly reduced body axis length compared to their
150 siblings, skinny appearance and with overall redness, especially in the head and gill
151 region (**Figure 1J**), which is not described in human NS patients and hence, may not
152 be related to NS.

153 Taken together, the NS Shp2^{D61G} mutant zebrafish we established
154 phenocopied several of the typical NS traits, such as stunted growth, craniofacial
155 defects, and heart defects. Similar to differences in symptoms observed in individual
156 human patients, the severity of the defects varied among individual Shp2^{D61G} mutant
157 zebrafish.

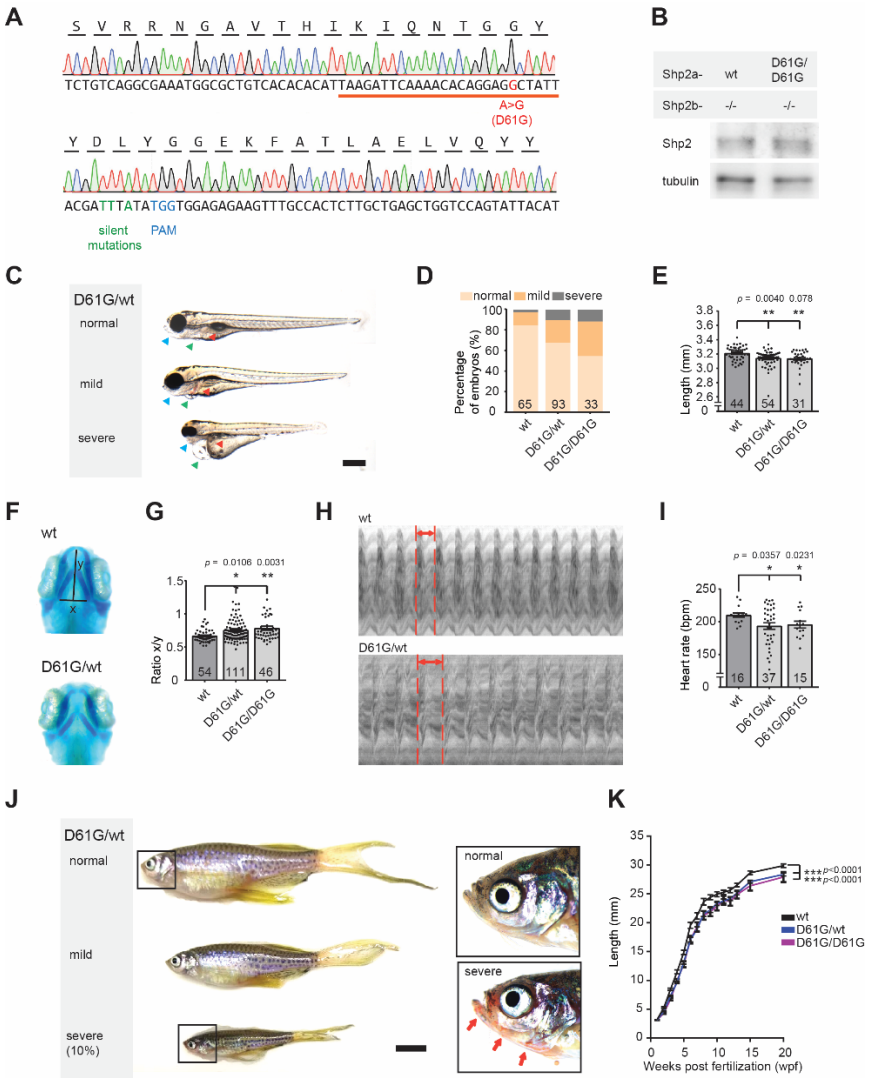

Figure 1. Shp2^{D61G} zebrafish display NS-like traits. (A) Sequencing trace derived from Shp2$^{D61G/D61G}$ zebrafish. Oligonucleotide sequence used to generate the model is underlined. Nucleotide substitutions for D61G mutation (red), silent mutations close to the PAM site (green) and the PAM site (blue) are indicated. **(B)** Immunoblot of Shp2 levels from 5 pooled Shp2a^{wt}Shp2b$^{-/-}$ or Shp2a$^{D61G/D61G}$Shp2b$^{-/-}$ embryos using antibodies for Shp2 and tubulin (loading control). **(C)** Representative images of typical Shp2^{D61G} zebrafish embryonic phenotypes at 5dpf. Blue arrows: jaw, green arrows: heart, red arrows: swim bladder. (**D)** Quantification of phenotypes of Shp2^{wt}, Shp2$^{D61G/wt}$ and Shp2$^{D61G/D61G}$ embryos scored as in **C** normal, mild and severe. **(E)** Body axis length of Shp2^{wt}, Shp2$^{D61G/wt}$ and Shp2$^{D61G/D61G}$ embryos at 5dpf. **(F)** Representative images of Alcian blue stained head-cartilage of 4dpf Shp2^{wt} and Shp2$^{D61G/wt}$ embryos. (x) width of ceratohyal, (y) distance to Meckel's cartilage. **(G)** Quantified craniofacial defects (x/y ratio). **(H)** Representative ventricular kymographs derived from high speed video recordings of beating hearts of 5dpf Shp2^{wt} and Shp2$^{D61G/wt}$ embryos. Red dotted lines indicate one heart period. **(I)** Heart rates derived from the ventricular kymographs. **(J)** Representative images of typical Shp2^{D61G} zebrafish adult phenotypes at 24wpf. Red arrows indicate skin redness in the jaw region. Scale bar is 0.5cm. Insets, zoom-in of boxed regions. **(K)** Body axis lengths of 10 Shp2^{wt}, 25 Shp2$^{D61G/wt}$ and 10 Shp2$^{D61G/D61G}$ zebrafish measured weekly between 5dpf and 20wpf of age. **(D,E,G,I)** Measurements originate from three distinct experiments. Number on bars: number of embryos. **(E,G,I,K)** Error bars: standard error of the mean (SEM), *p < 0.05; **p < 0.01, ***p < 0.001, ANOVA complemented by Tukey HSD.

158 **Increased numbers of HSPCs and myeloproliferative defects in Shp2^{D61G}**
159 **zebrafish embryos**
160 Next we explored hematopoietic abnormalities in the Shp2^{D61G} zebrafish
161 during embryonic development, corresponding to prenatal hematopoietic ontogeny in
162 human. We were not able to observe any effect of the Shp2^{D61G} mutation on primitive
163 hematopoiesis in embryos at 2dpf using WISH for markers of erythroid progenitors
164 (*gata-1*), myeloid progenitors (*pu.1*) and white blood cells (*l-plastin*) (**Figure 2-figure**
165 **supplement 1A**). On the other hand, a significant effect of the Shp2-D61G mutation
166 on definitive hematopoiesis was observed at 5dpf (**Figure 2**). First, the number of
167 HSPCs was determined using the Tg(*cd41:GFP*, *kdrl:mCherry-CAAX*) transgenic
168 line. CD41-GFP positive cells mark HSPCs when the GFP signal is low (CD41-
169 GFP^{low}) and thrombocytes when the GFP signal is high (CD41-GFP^{high}). An
170 increased number of CD41-GFP^{low} HSPCs was observed in the caudal
171 hematopoietic tissue region (CHT, corresponding to the fetal liver in human) and the
172 head kidney (corresponding to the bone marrow in human) of the mutant embryos
173 **(Figure 2A,B)**. Shp2^{D61G} mutation seems to affect both proliferation and apoptosis of
174 HSPCs, evident by an increase in CD41-GFP^{low} cells positive for phosphohistone H3
175 (pHis3), a marker for late G2 and M phase and a decrease in Acridine orange
176 positive cells in the CHT region, marking apoptotic cells (**Figure 2-figure**
177 **supplement 1B,C**). We observed an increase of *c-myb* positive cells, marking
178 HSPCs and of *l-plastin* positive cells, marking all white blood cells, in both CHT and
179 head kidney region of the Shp2^{D61G} mutants (**Figure 2C-F**). These latter cells appear
180 not to be lymphocytes, since the size of the *ikaros*-positive thymus, was not affected
181 (**Figure 2-figure supplement 1D,E**). On the other hand, the myeloid lineage was
182 markedly expanded, evident from the increase in the number of mpx-GFP positive
183 neutrophils (**Figure 2G,H**), and mpeg-mCherry positive macrophages (**Figure 2G,I**),
184 in Tg(*mpx:GFP, mpeg:mCherry*) double transgenic mutant embryos. Shp2^{D61G}
185 mutant embryos also displayed a mild decrease in the number of CD41-GFP^{high}-
186 positive thrombocytes, and the number of *β-globin* positive erythrocytes (**Figure 2-**
187 **figure supplement 1F-H)**. The observed defects in all different blood lineages
188 examined here were stronger in the homozygous Shp2$^{D61G/D61G}$ than heterozygous
189 Shp2$^{D61G/wt}$ embryos, supporting a dosage effect. One of the clinical hallmarks of
190 JMML is the hypersensitivity of myeloid progenitors to GM-CSF. GM-CSF is not

present in zebrafish, but stimulation of HSPCs in *ex vivo* colony forming assays in semi-solid media with Gcsfa or Gcsfb gives rise to colony-forming unit granulocyte (CFU-G) and colony-forming unit macrophage (CFU-M) type of colonies, similarly to GM-CSF stimulation in human, suggesting a compensatory role of Gcsfa/b for the missing GM-CSF in zebrafish (Oltova et al., 2018; Stachura et al., 2013). Compared to their wt siblings, colonies developed from the CD41-GFP^{low} cells isolated from the Shp2$^{D61G/wt}$ zebrafish embryos at 5dpf and exposed to Gcsfa were larger in size and number, demonstrating an enhanced CFU-G and CFU-M colony forming ability (**Figure 2J,K)**. Finally, we tested whether the observed myeloid expansion was reconstituted upon transplantation of the WKM cells harvested from Shp2$^{D61G/wt}$ animals in the Tg(*mpx:GFP, mpeg:mCherry*) background into the optically clear recipient *prkdc-/-* immunodeficient zebrafish (Moore et al., 2016). Animals injected with 1x10^5 mutant WKM cells (3/5) accumulated GFP- and mCherry- positive cells near the site of injection starting at 14 days and increasing until 28 days. By contrast, animals injected with WKM cells from control sibling animals with wt Shp2a (5/5) lacked any GFP- and mCherry- positive cells (**Figure 2L**).

Our findings suggest that the Shp2^{D61G} mutant zebrafish embryos develop multilineage hematopoietic defects during the definitive wave of fetal hematopoiesis, which originates in the HSPCs compartment. The observed defect is reminiscent of JMML-like MPN in human NS patients.

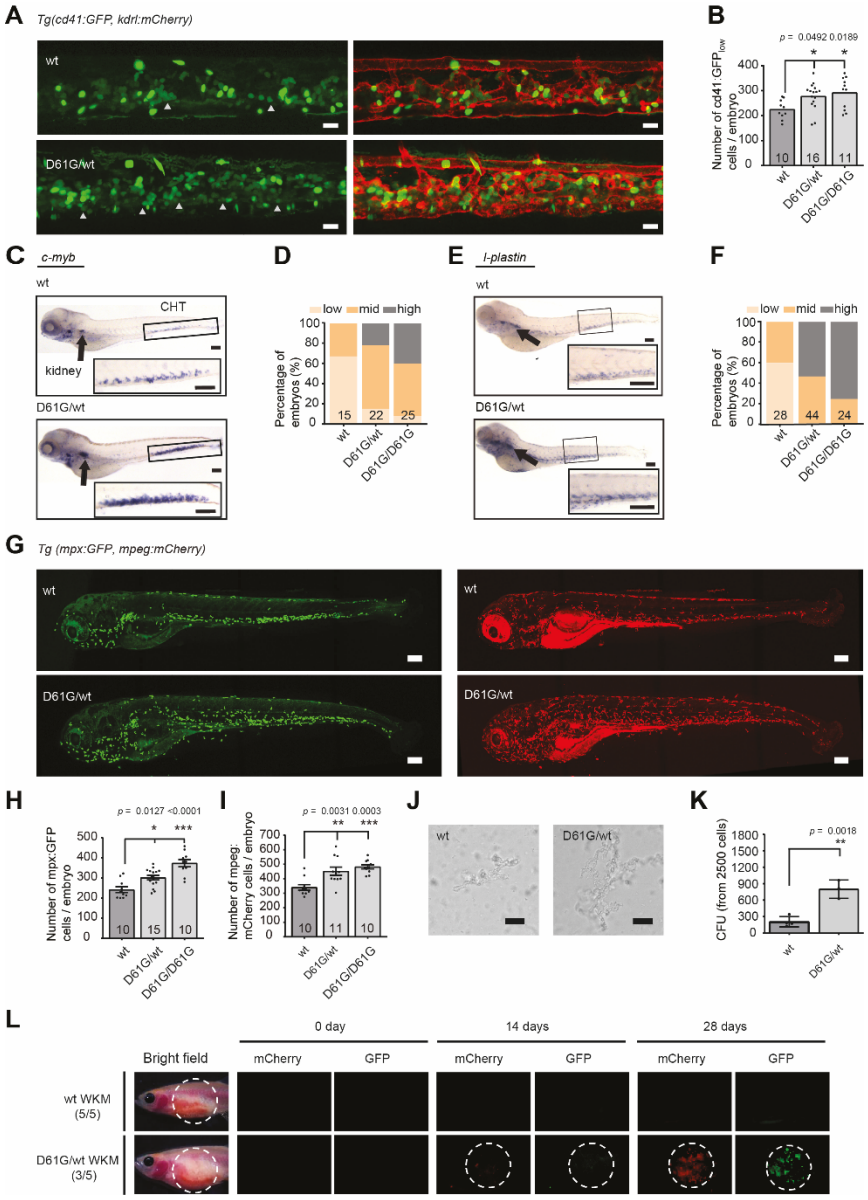

Figure 2. Shp2^{D61G} mutant zebrafish embryos display JMML-like MPN. (A) Representative images of the CHT region of Shp2^{wt} and Shp2^{D61G} zebrafish embryos in Tg(*cd41:GFP, kdrl:mCherry-CAAX*) background at 5dpf. *cd41:GFP^{low}* cells mark HSPCs and *cd41:GFP^{high}* cells thrombocytes. Grey arrow heads indicate *cd41:GFP^{low}* cells. Scale bar, 20µm. **(B)** The low intensity *cd41:GFP* positive cells in the CHT region were counted. **(C)** WISH of 5dpf Shp2^{wt} and Shp2$^{D61G/wt}$ embryos using *c-myb* specific probe. Head kidney (arrow) and CHT (box) are indicated; zoom-in in insert. Scale bars, 150µm. **(D)** Quantification of *c-myb* WISH. *C-myb* expression in Shp2^{wt}, Shp2$^{D61G/wt}$ and Shp2$^{D61G/D61G}$ embryos was scored as low, mid and high. **(E)** WISH of 5dpf Shp2^{wt} and Shp2$^{D61G/wt}$ embryos using *l-plastin* specific probe. Head kidney (arrow) and CHT (box) are indicated and zoom-in in insert. Scale bars,150µm. **(F)** Quantification of *l-plastin* expression in Shp2^{wt}, Shp2$^{D61G/wt}$ and Shp2$^{D61G/D61G}$ embryos scored as low, mid and high. **(G)** Representative images of Shp2^{wt} and Shp2^{D61G} zebrafish embryos in Tg(*mpx:GFP, mpeg:mCherry*) background at 5dpf. *Mpx:*GFP marks neutrophils and *mpeg*:mCherry macrophages. Scale bars,150µm. **(H,I)** Number of *mpx*:GFP and *mpeg*:mCherry positive cells per embryo. **(J)** Representative images of colonies developed from *cd41:GFP^{low}* cells isolated from the CHT of 5dpf Shp2^{wt} and Shp2$^{D61G/wt}$ zebrafish embryos, grown in methylcellulose with zebrafish cytokine Gcsfa for 2 days. Scale bar, 50µm. **(K)** Quantification of number of colonies from **J**, t-test. **(L)** WKM cells harvested from Shp2^{wt} and Shp2^{D61G} zebrafish in the Tg(*mpx:GFP, mpeg:mCherry*) background were injected into the peritoneum of adult *prkdc-/-* zebrafish. Recipients were monitored by fluorescence imaging. **(B,D,F,H,I,K)** Measurements originate from at least three distinct experiments. Number on bars: number of embryos. **(B,H,I,K)** Error bars represent SEM. *p < 0.05, **p<0.01, ***p<0.001. **(B,H,I)** ANOVA complemented by Tukey HSD.

211 **Myeloid bias is established during early differentiation of Shp2^{D61G} HSPCs**

212 In an effort to better understand the pathogenesis mechanisms in the
213 Shp2^{D61G} mutant HSPCs, single cell RNA sequencing was performed using SORT-
214 Seq on CD41-GFP^{low} cells derived from 5dpf Shp2^{wt}, Shp2$^{D61G/wt}$ and Shp2$^{D61G/D61G}$
215 zebrafish embryos in the Tg(*cd41*:*GFP*, *kdrl*:*mCherry-CAA*X) transgenic background
216 (**Figure 3A,B**). Unlike in human and mouse, the distinct compartments of HSPCs
217 cannot be isolated, due to lack of antibodies and transgenic lines. Thus, to group
218 cells based on their transcriptional program into specific HSPCs clusters,
219 unsupervised clustering was performed using the RaceID3 package (Herman et al.,
220 2018). Clusters were visualized by *t*-distributed stochastic neighbor embedding (*t*-
221 SNE) and 4 major clusters were further analyzed (**Figure 3C)**. Based on the
222 differentially expressed genes and GO term analysis, cells from Cluster 1 were
223 determined to be thrombocyte and erythroid progenitors, Cluster 2 HSC-like HSPCs,
224 Cluster 3 early myeloid progenitors and Cluster 4 monocyte/macrophage progenitors
225 (**Figure 3C, Figure 3-figure supplement 1A, Supplementary file 1**). A small
226 subset of cells in Cluster 4 represented more differentiated neutrophil progenitors
227 (**Figure 3-figure supplement 1B**).

228 HSPCs of either Shp2^{wt} or mutant Shp2$^{D61G/wt}$ and Shp2$^{D61G/D61G}$ genotypes
229 were present in all 4 major clusters, indicating that distinct HSPCs phenotypes were
230 maintained on a gene transcription level. However, the distribution of cells in clusters
231 differed among genotypes. An overrepresentation of mutant Shp2$^{D61G/wt}$ and
232 Shp2$^{D61G/D61G}$ cells was observed in the HSC-like HSPCs cluster and
233 monocytes/macrophages progenitors cluster, whereas these were underrepresented
234 in the thrombocyte and erythroid progenitors cluster **(Figure 3D,E**). To validate this
235 observation, we investigated the expression of *pu.1* and *alas2* markers in Shp2^{D61G}
236 embryos of different genotypes by WISH. In the single cell RNA sequencing dataset,
237 expression of *pu.1* and *alas2* was upregulated in the myeloid progenitors and
238 erythroid progenitors, respectively (**Figure 3F,I**). An increased number of *pu.1*
239 positive cells was detected by WISH in 5dpf old Shp2^{D61G} embryos compared to their
240 Shp2^{wt} siblings (**Figure 3G,H**), whereas the number of *alas2* positive cells in
241 Shp2^{D61G} mutants was decreased (**Figure 3J,K**).

242 Taken together, single cell RNA sequencing suggests that defects during
243 early differentiation of HSPCs to monocyte/macrophage progenitors and

244 erythroid/thrombocyte progenitors initiate the multilineage blood defect observed in

245 Shp2^{D61G} embryos, which recapitulates features of NS-JMML-like MPN.

246

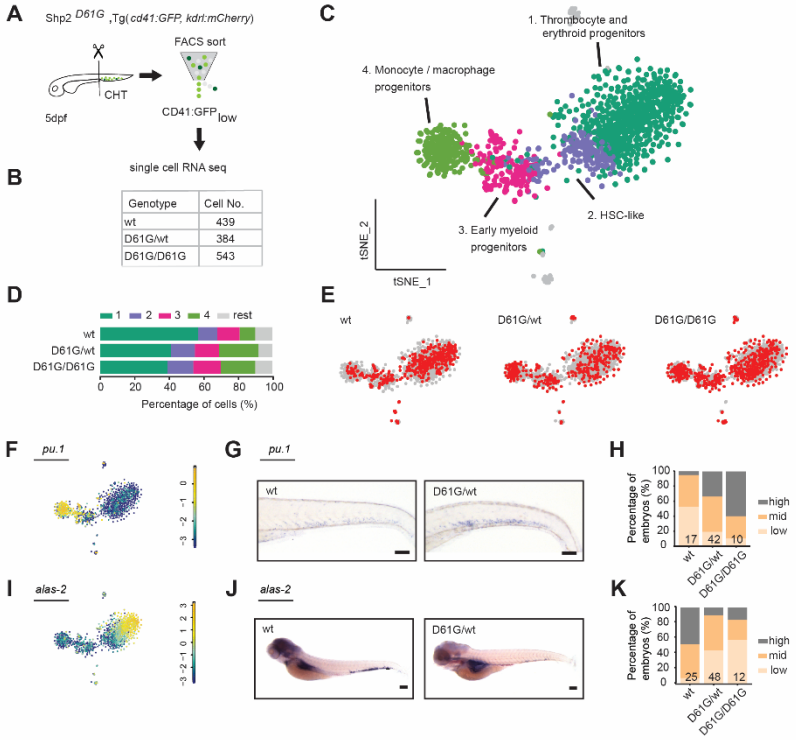

Figure 3. Single cell RNA sequencing of HSPCs reveals myeloid bias in Shp2^{D61G} embryos. (A) Schematic representation of the experimental procedure. At 5dpf, CHTs from Shp2^{wt}, Shp2$^{D61G/wt}$ and Shp2$^{D61G/D61G}$ embryos in Tg(*cd41:GFP, kdrl:mCherry-CAAX*) background were isolated. Cells were dissociated and separated by FACS, based on *cd41:GFP^{low}* expression, prior to single cell RNA sequencing, as described in the Materials and methods section. **(B)** Number of cells of distinct genotypes used in single cell RNA sequencing analysis. **(C)** Combined tSNE map generated using the cells of all three genotypes (Shp2^{wt}, Shp2$^{D61G/wt}$ and Shp2$^{D61G/D61G}$). Single cells from 4 major clusters are marked in dark green, blue, pink and green and their identities based on marker gene expression are indicated. Minor clusters are marked in grey. **(D)** Barplots showing the percentage of cells of Shp2^{wt}, Shp2$^{D61G/wt}$ and Shp2$^{D61G/D61G}$ genotype in distinct clusters. **(E)** Cells of distinct genotypes Shp2^{wt}, Shp2$^{D61G/wt}$ and Shp2$^{D61G/D61G}$ are visualized in tSNE maps in red. **(F)** tSNE maps showing log2-transformed read-counts of *pu.1*. **(G)** Representative images of the WISH staining for *pu.1* expression in 5dpf Shp2^{wt} and Shp2^{D61G} zebrafish embryos. Scale bar,100µm. **(H)** Expression of the *pu.1* marker scored as low, mid and high. **(I)** tSNE maps showing log2-transformed read-counts of *alas-2*. **(J)** Representative images of the WISH staining for *alas-2* expression in the tail region of 5dpf Shp2^{wt} and Shp2^{D61G} zebrafish embryos. Scale bar, 100µm. **(K)** Expression of the *alas-2* marker scored as low, mid and high. **(H,K)** Number on bars: number of embryos.

247

248

249 **Excessive proinflammatory response in monocyte/macrophage progenitors of**
250 **Shp2^{D61G} HSPCs**

251 We further analyzed the cluster of monocyte/macrophage progenitors, in
252 which we observed an overrepresentation of mutant Shp2^{D61G} cells **(Figure 4A)**.
253 Functional annotation of the differentially expressed genes and the GO-term
254 enrichment analysis revealed enhanced expression of proinflammatory genes in
255 mutant Shp2^{D61G} cells (**Figure 4A,B, Supplementary file 1**). Interestingly,
256 expression of inflammation-related genes, such as *gcsfa*, *gcsfb*, *il1b*, *irg1* and
257 *nfkbiaa,* was constrained to the cells of mutant Shp2^{D61G} genotype in the
258 monocyte/macrophage progenitors cluster, whereas the monocyte marker *timp2b*
259 was equally expressed by cells of distinct genotypes (**Figure 4B)**.

260 We next aimed to determine at which point the observed inflammatory
261 program initiated during the differentiation of HSC-like cells into
262 monocyte/macrophage progenitors. We used Monocle trajectory interference to
263 order cells from the four major clusters based on their differentiation state along the
264 pseudo-time. HSC-like cells were located at the start of the progression trajectory
265 and from there, two differentiation routes were determined, one leading to the
266 thrombocyte and erythrocyte progenitors, and the second one leading to the
267 monocyte/macrophage progenitors (**Figure 4C,D**). The route that includes HSC-like
268 cells, early myeloid progenitors and monocyte/macrophage progenitors was then
269 selected (**Figure 4C,D, Figure 4-figure supplement 1A**) and the expression of
270 inflammatory genes in distinct genotypes were computed along it (**Figure 4E, Figure**
271 **4-figure supplement 1B**). Expression of the monocyte marker *timp2b* started during
272 early differentiation of monocyte/macrophage progenitors. The level of *timp2b*
273 expression was similar in Shp2^{wt} and Shp2^{D61G} HSPCs Expression of the
274 inflammatory genes, *il1b*, *gcsfa*, *irg1*, *nfkbiaa* and *tnfa* started at a similar pseudo-
275 time as *timp2b* expression, but with a more robust expression in Shp2^{D61G} HSPCs
276 than in Shp2^{wt} HSPCs. Finally, high expression of IL-1β was validated in mutant
277 Tg(*il1b:eGFP*, *mpeg:mCherry*) transgenic embryos *in vivo*. IL-1β-eGFP positive cells
278 were more abundant in the CHT region of Shp2^{D61G} embryos than in wt embryos
279 (**Figure 4F)**.

280 Taken together, Shp2^{D61G} embryos display proinflammatory gene expression
281 in HSPCs, which is initiated during early differentiation of the monocyte/macrophage
282 progenitor cells.
283

284

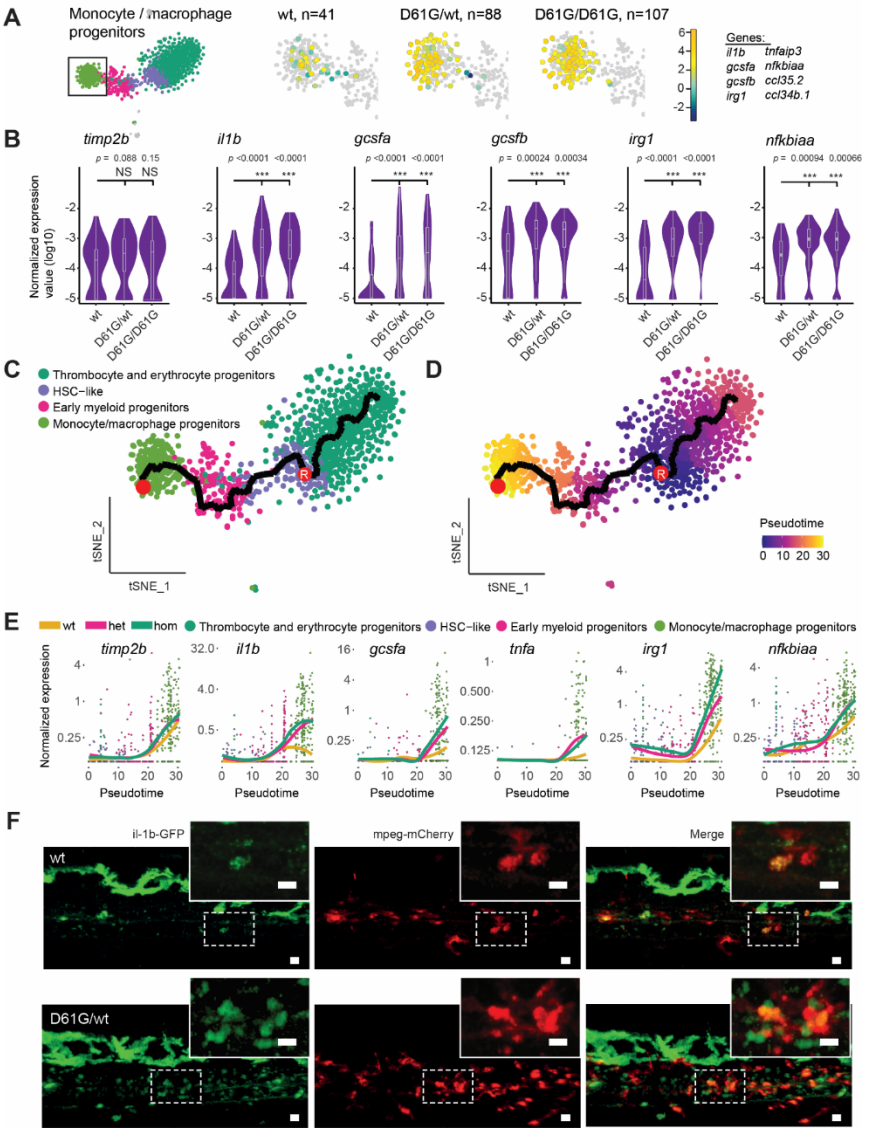

Figure 4. Inflammatory response in monocyte/ macrophage progenitors in Shp2^{D61G} embryos. **(A)** The monocyte/macrophage progenitors cluster (boxed on the tSNE map on left) was analyzed in detail. log2-transformed sum of read-counts of selected inflammation-related genes from the top 50 differentially expressed genes in the cells of the monocyte/macrophage progenitors cluster, with genotype and number of cells (n) indicated above. **(B)** Violin plots show the expression of specific genes in monocyte/macrophage progenitors of Shp2^{wt}, Shp2$^{D61G/wt}$ and Shp2$^{D61G/D61G}$ genotypes. NS, not significant, ***p < 0.001, t-test. **(C,D)** Monocle pseudotime trajectory of Shp2^{wt}, Shp2$^{D61G/wt}$ and Shp2$^{D61G/D61G}$ HSPCs differentiation superimposed on the four clusters and indicated by color in D. A route leading from HSC-like cells to monocyte/macrophage progenitors was selected and its root (R) and end are marked with red circles. **(E)** Pseudotemporal expression dynamics of specific genes along the selected route. The lines represent the smoothened regression of the moving average for Shp2^{wt}, Shp2$^{D61G/wt}$ and Shp2$^{D61G/D61G}$ genotypes. **(F)** *In vivo* imaging of the CHT region of Shp2^{wt} and Shp2$^{D61G/wt}$ zebrafish embryos in Tg(*il1b:eGFP*, *mpeg:mCherry*) background at 5dpf. Representative images are shown. The dashed line boxed region of CHT is zoom-in in insert. Scale bar is 10μm.

285 ***PTPN11* Somatic mutations induce inflammatory response genes in HSPCs of**
286 **JMML patients.**
287 We hypothesized that activating mutations in Shp2 may trigger an
288 inflammatory response in a similar way in sporadic JMML as we observed in
289 syndromic JMML-like MPN. To investigate this, we performed transcriptomic analysis
290 of the HSPCs compartments derived from bone marrows of sporadic JMML patients
291 with activating mutations in SHP2 (n=5) and age-matched healthy donors (n=7). The
292 SHP2 mutations in JMML HSPCs were distinct among patients and both HSCs and
293 progenitors were included (**Supplementary file 2**). Overall, we identified 1478
294 differentially expressed genes (DEGs) in HSPCs from JMML patients, compared to
295 the healthy donor HSPCs (**Figure 5A**, **Supplementary file 3**). The functional
296 analysis of DEGs using gene set enrichment analysis (GSEA) was performed to
297 systematically explore hallmark gene signatures specific for JMML HSPCs (**Figure**
298 **5B, Supplementary file 4**). Strikingly, altered expression of genes related to
299 inflammation was the most prominent, such as genes involved in TNFα signaling via
300 NFκB. The inflammatory response genes were significantly enriched in JMML
301 HSPCs (**Figure 5B-D**). De-regulation of genes related to proliferation (G2M
302 checkpoint, MYC targets and E2F targets) was evident in JMML HSPCs, suggesting
303 their decreased quiescence (**Figure 5B**).
304 We next studied whether the inflammatory-related gene signature overlaps
305 between HSPCs from zebrafish NS/JMML-like MPN model and human JMML. GSEA
306 revealed that human orthologs of the top 100 DEGs found in the zebrafish
307 monocyte/macrophage progenitor cells were enriched significantly in patient JMML
308 HSPCs (**Figure 5E**). Some of the top overexpressed inflammation-associated genes
309 in JMML patients, such as TNF and MARCKSL were also overexpressed in
310 NS/JMML-like MPN mutant zebrafish embryos compared to the wt (**Figure 5F,G**).
311 3D PCA analysis visualized that these zebrafish signature genes were able to clearly
312 segregate HSPCs from JMML patients and healthy donors (**Figure 5H**). These
313 findings suggest that mutant, activated SHP2 triggers proinflammatory gene
314 expression in HSPCs both in sporadic JMML patients and in our zebrafish model of
315 syndromic JMML-like MPN in a similar manner, suggesting a common underlying,
316 endogenously driven process.

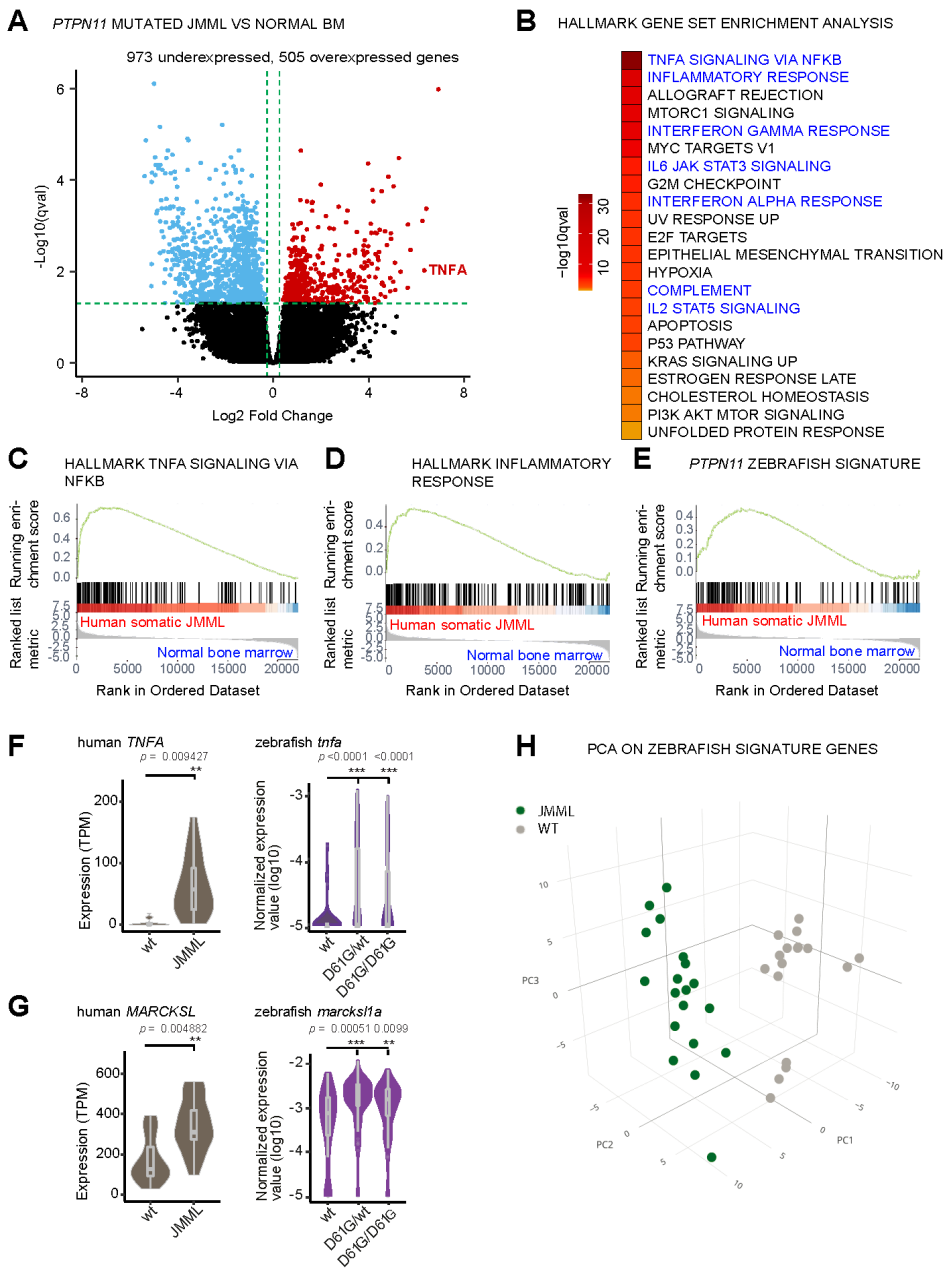

317

318

Figure 5. Similar molecular signatures in HSPCs from human JMML patients and zebrafish Shp2^{D61G} embryos. (A) Volcano plot of differentially expressed genes of HSPCs derived from bone marrow of JMML patients with *PTPN11* mutations (n=5) and healthy bone marrow (n=7). Underexpressed genes are marked in blue and overexpressed genes are marked in red. *TNFA* expression is highlighted. Green dashed lines indicate the significance level. **(B)** GSEA for the MSigDB's hallmark gene sets in HSPCs from JMML compared to normal human age-matched bone marrow. GSEA plots for TNFA_SIGNALING_VIA_NFKB **(C)**, INFLAMMATORY RESPONSE **(D)**, and the custom Zebrafish signature based on the top 100 human orthologous of genes upregulated in monocyte/macrophage progenitor cluster of zebrafish HSPCs **(E)**. Violin plots show the expression of *TNFA* **(F)** and *MARCKSL* **(G)** in either human wt vs. JMML HSPCs, and zebrafish Shp2^{wt} vs. Shp2$^{D61G/wt}$ and Shp2$^{D61G/D61G}$ monocyte/macrophage HSPC progenitors. **p<0.01, ***p < 0.001, t-test. **(H)** PCA for the 100 genes included in the custom zebrafish signature. Green dots represent *PTPN11* mutated JMML, gray ones represent normal human age-matched bone marrow. PC1: 19% of the variance, PC2: 16% of the variance, PC3: 14% of the variance.

319 **Inhibition of the proinflammatory response ameliorates the JMML-like MPN**
320 **phenotype**

321 To investigate the role of the inflammatory response in the blood defect, we
322 assessed the effect of dexamethasone in Shp2^{D61G} embryos. Dexamethasone is an
323 anti-inflammatory agent, which is known to suppress the inflammatory response in
324 the monocyte/macrophage lineage (Ehrchen et al., 2019; Xie et al., 2021). In
325 parallel, inhibitors of the known Shp2-associated signaling pathways were used,
326 targeting MEK (CI1040) or PI3K (LY294002) (Tajan et al., 2015). Shp2^{D61G} embryos
327 were exposed to inhibitors continuously from 2 to 5 dpf (**Figure 6A**). Both CI1040
328 and LY294002 led to a robust reduction in expansion of both HSPCs and myeloid
329 lineage in mutant embryos, measured by WISH using markers for *c-myb* and *l-*
330 *plastin* (**Figure 6B,C**), demonstrating that the NS-associated blood development
331 defect in Shp2^{D61G} embryos was largely caused by overactivation of the RAS-MAPK
332 and PI3K pathways as expected.

333 To our surprise, dexamethasone reduced *c-myb* and *l-plastin* expression to a
334 similar extent as CI1040 and LY294002 (**Figure 6B,C**), indicating a profound role for
335 the inflammatory response in the pathogenesis of NS-associated blood defects. We
336 then examined whether dexamethasone treatment affected the expanded myeloid
337 lineage in Shp2^{D61G} embryos by determining the number of neutrophils and
338 macrophages, in the Tg(*mpx:GFP, mpeg:mCherry*) double transgenic mutant
339 embryos (**Figure 6D-F**). Upon dexamethasone treatment, the number of *mpx*-GFP
340 and *mpeg*-mCherry positive cells decreased in Shp2^{D61G} embryos to similar levels as
341 observed in Shp2^{wt} embryos, indicating that dexamethasone treatment rescued the
342 expansion of the myeloid lineage in Shp2^{D61G} embryos. Dexamethasone did not
343 significantly alter the number of neutrophils or macrophages in wild type embryos
344 (**Figure 6D-F**). Finally, the expression of proinflammatory genes, such as *tnfa*, *il1b*
345 and *gcsfb* in Shp2^{D61G} embryos was reduced in response to dexamethasone
346 treatment to levels observed in Shp2^{wt} embryos (**Figure 6G**).

347 Taken together, we observed a proinflammatory phenotype of the
348 macrophage/ monocyte lineage in Shp2^{D61G} mutant zebrafish, which was established
349 early during HSPCs differentiation. The anti-inflammatory agent dexamethasone
350 largely rescued the hematopoietic defects, suggesting that the inflammatory
351 response in Shp2^{D61G} mutant zebrafish had a causal role in the pathogenesis of the
352 NS/JMML-like MPN blood phenotype.

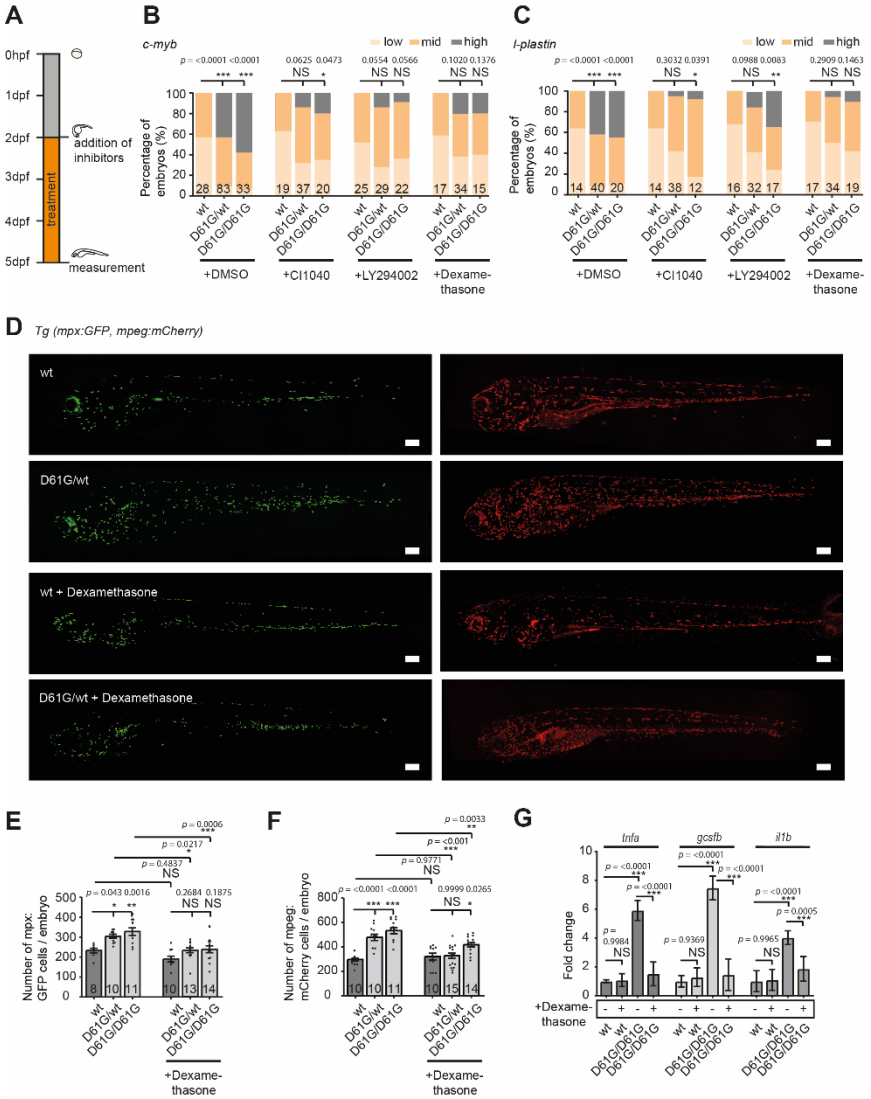

Figure 6. Anti-inflammatory treatment of zebrafish Shp2^{D61G} embryos ameliorates the JMML-like MPN phenotype. (A) Schematic overview of the treatments with MEK inhibitor CI1040, PI3K inhibitor LY294002 and anti-inflammatory corticosteroid dexamethasone. Embryos were continuously treated from 48hpf until 5dpf, when either WISH, confocal imaging or RT-qPCR was performed. **(B,C)** WISH staining for the expression of the *c-myb* and *l-plastin* markers was scored as low, mid and high. Measurements originate from at least three distinct experiments. Number on bars: number of embryos. NS, not significant; *p < 0.05, **p<0.01, ***p<0.001, Chi-squared test. **(D)** Representative images of 5 dpf Shp2^{wt} and Shp2^{D61G} zebrafish embryos in Tg(*mpx:GFP, mpeg:mCherry*) background without and with dexamethasone treatment. Scale bars,150µm. **(E,F)** Number of *mpx*:GFP and *mpeg*:mCherry positive cells per embryo. Number on bars: number of embryos. Error bars represent SEM. **(G)** Expression of *tnfa*, *gcsfb* and *il1b* genes determined by RT-qPCR in Shp2^{wt} and Shp2$^{D61G/D61G}$ zebrafish embryos without and with dexamethasone treatment at 5dpf, normalized to *ef1a* expression. Standard deviation of 4 samples in duplicates for each condition are shown. **(E,F,G)** *p < 0.05, **p<0.01, ***p<0.001. ANOVA complemented by Tukey HSD.

353

354

Discussion

To investigate the timing and pathophysiology of mutant SHP2-related myeloproliferative defects, we explored the transcriptomes of HSPCs with activating mutations in SHP2, derived from sporadic JMML patients and syndromic NS/JMML-like MPN zebrafish embryos, respectively. Proinflammatory gene expression was evident both in HSPCs from JMML patients and mutant zebrafish. It should be noted that the type of data is different, bulk sequencing of the human samples and single cell sequencing of the zebrafish material. In addition, the source of the material is distinct, FACS-sorted CD41-GFP^{low} HSPCs from zebrafish embryos and immunophenotypically FACS-sorted postnatal HSCs and progenitors from human. Moreover, genotypically, the samples differed in that the zebrafish carried a single Shp2 mutation (D61G) and the human JMMLs carried distinct activating SHP2 mutations even with additional mutations. Therefore, it is not surprising that the ranking of overexpressed inflammatory genes in HSPCs from mutant zebrafish and human JMML patients was not identical. Nevertheless, the similarity of the proinflammatory signatures revealed by GSEA between these diverging samples is striking.

Already early studies reported high levels of proinflammatory cytokines, such as IL-1β, TNF-α, GM-CSF, in JMML patients plasma (Bagby et al., 1988; Freedman et al., 1992). However, little is known about the cellular origin of the proinflammatory status, its pathophysiological role and therapeutic potential. The inflammatory response may be initiated in a cell autonomous way or in response to signals from the microenvironment. Dong et al. suggested that IL-1β is secreted by differentiated monocytes which get recruited upon secretion of the Chemokine, CCL3, by cells of the bone marrow microenvironment containing activating SHP2 mutations. However, the levels of CCL3 in the bone marrow of four NS patients varied (Dong et al., 2016). Furthermore, a microenvironment-driven inflammatory response would not explain high levels of cytokines in sporadic JMML, where niche cells are not mutated. On the other hand, recent reports indicate that JMML leukemia stem cells are heterogeneous but confined to the HSPCs compartment, defining JMML HSPCs as the origin of the disease (Caye et al., 2019; Louka et al., 2021). The pseudotime analysis of inflammatory genes in zebrafish HSPCs indicated that the initiation of the proinflammatory program happens during early differentiation of HSPCs towards the

388 monocyte/macrophage progenitor lineage in Shp2^{D61G} embryos. The limited number
389 of human patients included in our analysis allowed us to establish that the HSPCs
390 compartment from JMML patients showed an inflammatory response, but not which
391 lineage. Transcriptomic analysis of individual progenitor lineages from additional
392 patients will be required to conclude which cell type displayed an inflammatory
393 response. Our data suggest that proinflammatory reprogramming of the
394 monocyte/macrophage lineage might be endogenously driven at least in part, and
395 detailed mechanisms remain to be elucidated in the future.

396 To our knowledge, the Shp2^{D61G} mutant zebrafish we developed is the first NS
397 zebrafish model carrying an activating Shp2 mutation at its endogenous locus
398 generated by CRISPR/Cas9-based knock-in technology. Strikingly, phenotypes
399 developed by the Shp2^{D61G} zebrafish corroborate closely with the phenotypes
400 displayed by human NS patients and the existing NS mouse models **(Figure 1)**. Our
401 model presents an exciting novel tool for deciphering pathogenesis mechanisms of
402 NS with its complex traits and for finding novel therapies for this as yet poorly
403 treatable condition.

404 NS children with D61G mutation have a higher predisposition to develop
405 JMML(-like MPN), and comparably Shp2^{D61G} zebrafish embryos displayed typical
406 JMML-like MPN characteristics, such as expansion of the myeloid lineage, increased
407 sensitivity to gcsfa, mild anemia and thrombocytopenia **(Figure 2)**. Furthermore, the
408 observed blood defect was transplantable to secondary recipients and the disease
409 originated in HSPCs, which displayed aberrant proliferation and apoptosis. Given the
410 importance of fetal hematopoiesis during JMML(-like MPN) development, the
411 zebrafish Shp2^{D61G} mutant represents a reliable and unique model for JMML-like
412 MPN, which allows us to study hematopoietic defects caused by mutant Shp2 during
413 the prenatal development for the first time. Our results suggest that the JMML-like
414 MPN defect is initiated at the CHT, which is the counterpart of fetal liver in human.
415 Here we observed expanded HSPCs, which displayed aberrant proliferation and
416 apoptosis. We further characterized the transcriptomes of HSPCs specifically
417 originating from the CHT, and studied their response to inhibitor treatments directly
418 at the CHT. Striking similarities between the patient and zebrafish HSPCs
419 transcriptomes indicate that the Shp2^{D61G} zebrafish model is an exciting preclinical
420 model for *in vivo* drug screens at relevant developmental time points, in a high
421 throughput manner.

422 The only effective treatment of JMML is allogeneic stem cell transplantation,
423 which has a high relapse rate of 50%. Hence, there is a great need for other means
424 of therapeutic intervention. The role of inflammation as one of the drivers in myeloid
425 leukemogenesis is emerging (Arranz et al., 2017; Craver et al., 2018). Here we
426 demonstrate that dampening inflammation using the glucocorticoid dexamethasone,
427 partially rescued the observed blood phenotype in Shp2^{D61G}, suggesting that the
428 inflammatory response evoked in the cells of myeloid/macrophage lineage was an
429 important driver of the NS/JMML-like blood defect and might be a potential drug
430 target for both sporadic and syndromic JMML(-like MPN). To our surprise, targeting
431 inflammation reversed the blood defect to a similar extent as the MAPK and PI3K
432 pathway inhibitors, emphasizing not only the crucial role of inflammation during
433 JMML pathogenesis, but also its strong therapeutic potential. Since anti-
434 inflammatory therapies are non-invasive and widely available, targeting inflammation
435 might represent a novel avenue for JMML treatment, either alone or in combination
436 with other therapies.
437 In conclusion, we observed striking similarities in expression patterns of
438 HSPCs from sporadic human JMML patients with an activating SHP2 mutation and
439 HSPCs from an engineered zebrafish model with an activating NS-associated
440 mutation in Shp2. Particularly genes associated with the inflammatory response
441 were upregulated and strikingly, pharmacological inhibition of the inflammatory
442 response ameliorated JMML-like MPN in the zebrafish model, suggesting this may
443 be a first step for therapeutic intervention in human patients.

Materials and methods

Zebrafish husbandry

All procedures involving experimental animals were approved by the animal experiments committee of the Royal Netherlands Academy of Arts and Sciences (KNAW), Dierexperimenten commissie protocol HI18-0702, and performed under the local guidelines in compliance with national and European law. The following zebrafish lines were used in the study: Tübingen longfin (TL, wild type), Tg(*cd41:GFP, kdrl:mCherry-CAAX*) (Hogan et al., 2009; Lin et al., 2005), Tg*(mpx:GFP, mpeg:mCherry)* (Ellett et al., 2011; Renshaw et al., 2006), TgBAC(*il1b:eGFP*)sh445 (Ogryzko et al., 2019), *ptpn11b-/-* (Bonetti et al., 2014)*prkdc-/-* (Moore et al., 2016) and the novel Shp2^{D61G} zebrafish line. Raising and maintenance of zebrafish was performed according to (Aleström et al., 2020; Westerfield, 2000). When required, pigmentation of embryos was blocked by adding phenylthiourea (PTU) (Sigma Aldrich, St. Louis, MO, USA, Ref: P7629) at a concentration of 0.003% (v/v) to the E3 medium at 24hpf.

Patient material

All children's samples were obtained after parents had given their written informed consent. Experiments were approved by the institutional review board of the French Institute of Health and Medical Research (INSERM) (IORG0003254) in accordance with the Helsinki declaration. Healthy children bone marrows were obtained from intrafamilial BM transplantation donors and used with the approval of the Institutional Review Board of "Hôpitaux Universitaires Paris Nord Val-de-Seine," Paris 7 University, AP-HP), (IRB: 00006477), in accordance with the Helsinki declaration. HSPCs fractions were FACS sorted according to immunophenotypic signature as previously described (Caye et al., 2019), from PTPN11^{mut} JMML (n=5) and healthy children bone marrow (n=7). Age, sex, mutations and fractions available for each sample (Hematopoietic stem cells (HSCs), multipotent progenitors (MPPs), common myeloid progenitors (CMPs), granulocyte-macrophage progenitors (GMPs), and megakaryocyte-erythroid progenitors (MEPs)) are indicated in **Supplementary file 2**.

Generation of the Shp2^{D61G} zebrafish line

The Shp2^{D61G} zebrafish line was generated using the previously described CRISPR/Cas9-based knock-in approach (Tessadori et al., 2018). The sgRNA

477 targeting exon 3 of the *ptpn11a* gene (5'- GGAGACTATTACGACCTGTA-3') was
478 designed using the CHOP-CHOP database (http://chopchop.cbu.uib.no/), further
479 processed according to the previously published guidelines (Gagnon et al., 2014)
480 and finally transcribed using the Ambion MEGAscript T7 kit (TermoFisher Scientific,
481 Waltham, MA, USA, Ref: AMB13345). The sgRNA, constant oligonucleotide and
482 template oligonucleotide were all generated by Integrated DNA Technologies (IDT,
483 Coralville, IA, USA) as standard desalted oligos and template oligonucleotide was
484 further purified using the QIAquick Nucleotide Removal Kit (Qiagen, Hilden,
485 Germany, Ref: 28304). The oligonucleotide used for the homology repair is 59
486 nucleotides long and besides the D61G mutation, contains three additional silent
487 mutations in proximity of the PAM site. The sequence of template oligonucleotide is
488 5'-
489 GAGTGGCAAACTTCTCTCCACCATATAAATCGTAATAGCCTCCTGTGTTTTGAAT
490 CTTA-3'. Tübingen longfin wt zebrafish embryos at the one-cell-stage were injected
491 directly in the cell with 1 nl of the injection mixture containing 18.75 ng/ml of sgRNA,
492 37.5 ng/ml of template oligonucleotide and 3.6 mg/ml of Cas9 protein in 300 mM
493 KCl. Cas9 protein was a gift from the Niels Geijsen laboratory at the Hubrecht
494 Institute. The injected embryos were grown into the adulthood. F0 generation
495 zebrafish were outcrossed with the wt zebrafish. DNA extracted from the 12 distinct
496 1dpf old F1 generation embryos was screened for the correct insertion of the
497 template oligonucleotide. Screening was done by Sanger sequencing (Macrogen
498 Europe B.V., Amsterdam, The Netherland) of the 225 bp long PCR product
499 encompassing the genomic regions of the CRISPR target sites, which was
500 generated using the forward 5'-TCATCTCCTCACTAGGCGAAAT-3' and reverse
501 primer 5'- TATGTATGTGCTCACCTCTCGG-3'. The efficiency of the knock-in was
502 1.8% (1 founder zebrafish in 54 screened primary injected zebrafish). F1 generation
503 was then established from the F0 founder. F1 generation adults were finclipped and
504 sequenced for the presence of the mutation. All experiments were performed in
505 zebrafish embryos and adults from the F3 and F4 generation. For all of the
506 experiments except single cell RNA sequencing and RT-qPCR, embryos were
507 siblings derived from an incross of Shp2$^{D61G/wt}$ animals. After the experimental
508 procedure, embryos were lysed and genotyped by sequencing as described above.
509 Western blotting was performed as previously described (Hale & den Hertog, 2017)

510 using the Shp2 (Santa Cruz Biotechnology, Dallas, TX, USA, Ref: SC-280) and β-
511 tubulin (Merck Millipore, Burlington, MA, USA Ref: CP06) antibodies.

512 **Phenotyping of the NS traits**

513 Body axis lengths were measured from the tip of the head to the end of the trunk in
514 the bright-field images of laterally positioned embryos, larva and adults, which were
515 anesthetized in 0.1% MS-222. Alcian blue (Sigma Aldrich, Ref: A5268) staining was
516 performed as previously described (Paardekooper Overman et al., 2014), on PTU-
517 treated 4dpf old embryos, which were anesthetized in 0.1% MS-222 and fixed in 4%
518 PFA overnight. Embryos were positioned on their back in 70% glycerol in PBS and
519 imaged with Leica M165 FC stereomicroscope (Leica Microsystems, Wetzlar,
520 Germany. Analysis was performed in ImageJ. *In vivo* high-speed brightfield imaging
521 of the embryonic hearts from PTU-treated embryos at 5dpf, which were anesthetized
522 in 0.1% MS-222 and embedded in 0.3% UltraPure agarose (Thermo Fisher
523 Scientific, Waltham, MA, USA) prepared in E3 medium containing 16 mg/ml MS-222.
524 Measurements were performed at 28°C using a Leica DM IRBE inverted light
525 microscope (Leica Microsystems) with a Hamamatsu C9300-221 high-speed CCD
526 camera (Hamamatsu Photonics, Hamamatsu, Japan). Imaging was conducted at
527 150 frames per seconds (fps) using Hokawo 2.1 imaging software (Hamamatsu
528 Photonics) for a period of 10 seconds (approximately 30 cardiac cycles). Heart rate
529 measurements and contractility parameters were analysed using ImageJ. Volumes
530 were analysed using ImageJ by drawing an ellipse on top of the ventricle at end-
531 diastole and end-systole. Averages of three measurements per heart were
532 determined. End diastolic and end systolic volume (EDV/ESV) were calculated by:
533 (4/3)*(π)*(major axis/2)*((minor axis/2)^2). Stroke volume (SV) by: EDV-ESV.
534 Ejection fraction (EF) by: (SV/EDV)*100. Cardiac output (CO) by: SV*Heart rate.

535 **Whole mount *in situ* hybridization**

536 PTU-treated embryos were anesthetized in 0.1% MS-222 (Sigma Aldrich, Ref:
537 A5040) and fixed in 4% PFA for at least 12h at 4°C. *WISH* was performed as
538 described in (Thisse et al., 1993)**.** Probes specific for *myl7*, *vhmc* and *ahmc* were
539 described in (Bonetti et al., 2014). Probes specific for *c-myb*, *l-plastin*, *pu.1*, *gata1*,
540 *ikaros*, *b-globin* and *alas-2* were described in (Choorapoikayil et al., 2014; Hu et al.,
541 2014)**.** Subsequently, embryos were mounted in 70% glycerol in PBS and imaged
542 with Leica M165 FC stereomicroscope (Leica Microsystems). Images were

543 processed in ImageJ (U. S. National Institutes of Health, Bethesda, MD, USA).
544 Abundance of the probe signal was scored as low, mild or high.

545 **Inhibitors treatment**

546 PTU-treated embryos were incubated with either 0.15μM of CI1040 (Sigma Aldrich,
547 Ref: PZ0181), 4μM LY294002 (Sigma Aldrich, Ref: L9908) or 10μM of
548 Dexamethasone (Sigma Aldrich, Ref: D4902) continuously from 48hpf until 5dpf in
549 the same medium. At 5dpf embryos were either fixed and half of the embryos was
550 processed for WISH using probe specific for *c-myb* and the other half using probe
551 specific for *l-plastin*, or snap-frozen and processed for RT-qPCR, while the live
552 embryos in Tg*(mpx:GFP, mpeg:mCherry)* transgenic background were imaged by
553 confocal microscopy

554 **Confocal microscopy**

555 All confocal imaging was performed on a Leica SP8 confocal microscope (Leica
556 Microsystems). Embryos were mounted in 0.3% agarose. Live embryos were
557 anesthetized in MS-222. Whole embryos were imaged using a 10X objective and z-
558 stack step size of 3μm, while the CHT area with 20X objective and z-stack step size
559 of 1μm. The number of CD41-GFP^{low} cells was determined by imaging the CHT of
560 the living 5dpf old embryos of the Shp2^{wt}, Shp2$^{D61G/wt}$ and Shp2$^{D61G/D61G}$ siblings in
561 the Tg(*cd41:GFP, kdrl:mCherry-CAAX*) transgenic background, while the number of
562 CD41-GFP^{high} cells was determined by imaging whole embryos, which were fixed for
563 2h in 4% PFA prior to imaging. To determine the number of mpx-GFP and mpeg-
564 mCherry cells, whole live 5dpf old embryos of the Shp2^{wt}, Shp2$^{D61G/wt}$ and
565 Shp2$^{D61G/D61G}$ line in the Tg*(mpx:GFP, mpeg:mCherry)* transgenic background were
566 imaged. Imaris V9.3.1 (Bitplane, Zurich, Switzerland) was used to reconstruct 3D
567 images and count individual GFP and/or mCherry positive cells.

568 **Phosphorylated Histone 3 (pHis3) staining**

569 PTU-treated 5dpf old Shp2^{D61G} embryos in the Tg(*cd41:GFP, kdrl:mCherry-CAAX*)
570 transgenic background were fixed in 2% PFA overnight and stained as described in
571 (Choorapoikayil et al., 2012). Primary pHis3 antibody (1:500 in blocking buffer,
572 Abcam, Cambridge, UK, Ref: ab5176) and secondary GFP antibody (1:200 in
573 blocking buffer, Aves Labs Inc. Tigard, OR, USA, GFP-1010) were used. Embryos
574 were mounted in 0.3% agarose, their CHT was imaged using the SP8 confocal
575 microscope and 3D images were subsequently reconstructed using Imaris.

576 **Acridine orange staining**

577 PTU-treated embryos at 5dpf were incubated in 5µg/ml of Acridine orange (Sigma
578 Aldrich, Ref: A6014) in E3 medium, for 20 minutes at room temperature. They were
579 then washed 5 times for 5 minutes in E3 medium, anesthetized in MS-222 and
580 mounted in 0.3% agarose. Whole embryos were imaged with SP8 confocal
581 microscope and 3D images were reconstructed using Imaris.

582 **Colony forming assay**

583 The CD41-GFP^{low} cell population isolated from CHTs of Shp2^{wt}, Shp2$^{D61G/wt}$ embryos
584 at 5dpf was FACS sorted. 250 µl of solution containing 2 500 cells, media prepared
585 as described in (Svoboda et al., 2016)**,** and 100 ng/ml of granulocyte colony
586 stimulating factor a (Gcsfa, gift from the Petr Bartunek lab, Institute of Molecular
587 Genetics, Academy of Sciences of the Czech Republic v.v.i. Prague) was plated per
588 well of a 96 well plate in a triplicate. Cells were grown in humidified incubators at
589 32°C, 5% CO_2. After 6 days colonies were imaged and counted using the EVOS
590 microscope (Termo Fisher Scientific).

591 **Quantitative reverse transcription PCR (RT-qPCR)**

592 Zebrafish siblings of either Shp2^{wt} or Shp2$^{D61G/D61G}$ genotypes were crossed to
593 generate embryos of Shp2^{wt} and Shp2$^{D61G/D61G}$ genotype. At 5dpf, 5 embryos of the
594 same condition were pooled and snap frozen in liquid nitrogen. Total RNA was
595 extracted from embryos using the TRIzol reagent according to the manufacturer's
596 instructions (Thermo Fisher Scientific, Invitrogen, Ref: 15596018). cDNA synthesis
597 was performed from 800 ng of RNA using the SuperScript® III First-Strand kit
598 (Thermo Fisher Scientific, Invitrogen, Ref: 12574018). RT-qPCR was performed with
599 an CFX Connect Real-Time system (Bio-Rad Laboratories Inc., Hercules, CA, USA)
600 using FastStart Universal SYBR Green Master (ROX) (Roche, Basel, Switzerland)
601 and 1:20 dilution of cDNA. Reaction mixtures were incubated for 10 min at 95°C,
602 followed by 42 cycles of product amplification (15 seconds at 95°C and 1 minute at
603 58°C). For each condition 4 samples were used in duplicate. Gene expression was
604 normalized against the expression of *ef1a* for each mRNA. The following primers
605 were used: *ef1a* forward, 5'-GAGAAGTTCGAGAAGGAAGC-3'; *ef1a* reverse, 5'-
606 CGTAGTATTTGCTGGTCTCG-3'; *tnfa* forward, 5'-
607 AGACCTTAGACTGGAGAGATGAC-3'; *tnfa* reverse, 5'-
608 CAAAGACACCTGGCTGTAGAC-3'; *gcsfb* forward, 5'-

609 AGAGAACCTACTGAACGACCT-3'; *gcsfb* reverse, 5'-
610 CTTGAACTGGCTGAGTGGAG-3'; *il1b* forward, 5'-
611 GAACAGAATGAAGCACATCAAACC-3'; *il1b* reverse, 5'-
612 ACGGCACTGAATCCACCAC-3'.

613 **Transplantation experiments**

614 Zebrafish kidney marrow transplantation were performed as previously described
615 (Moore et al., 2016; Tang et al., 2014). In short, tissues were isolated from donor
616 Shp2$^{D61G/wt}$ or wild type animals in the Tg(*mpx:GFP, mpeg:mCherry*) background
617 following Tricaine (Western Chemical, Brussels, Belgium) overdose. Excised tissues
618 from dissected fish are placed into 500 µl of 0.9x PBS + 5% FBS on a 10-cm Petri
619 dish. Single-cell suspensions were obtained by maceration with a razor blade,
620 followed by manual pipetting to disassociate cell clumps. Cells were filtered through
621 a 40-µm Falcon cell strainer, centrifuged at 1,000 *g* for 10 min, and resuspended to
622 the 2 x 10^7 cells/ml. 5-µl suspension containing 10^5 kidney marrow cells were
623 injected into the peritoneal cavity of each recipient fish using a 26s Hamilton 80366
624 syringe. Cellular engraftment was assessed at 0, 7, 14, 28 dpt by epifluorescence
625 microscopy.

626 **Isolation of CD41-GFP^{low} cell population and single-cell RNA sequencing**

627 Zebrafish siblings of either Shp2^{wt} or Shp2$^{D61G/D61G}$ genotypes were crossed to
628 generate embryos of Shp2^{wt}, Shp2$^{D61G/wt}$ and Shp2$^{D61G/D61G}$ genotype. From 24hpf
629 onwards embryos were grown in PTU-containing medium. The CHTs of
630 approximately 50 randomly selected Shp2^{wt}, Shpt$^{D61G/wt}$ and Shp2$^{D61G/D61G}$ embryos
631 in Tg(*cd41:GFP, kdrl:mCherry-CAAX*) transgenic background at 5dpf were dissected
632 and CHTs of the same genotype were pooled in Leibovitz-medium (Thermo Fisher
633 Scientific, Gibco, Ref: 11415049). After washing with PBS0 the CHTs were
634 dissociated with TryplE (Thermo Fisher Scientific, Gibco, Ref: 12605036) for 45
635 minutes at 32°C. The resulting cell suspension was washed with PBS0, resuspended
636 in PBS0 supplemented with 2mM EDTA, 2% FCS and 0.5µg/ml DAPI (Sigma
637 Aldrich, Ref: D9542) and passed through a 40µm Falcon cell strainer. DAPI staining
638 was used to exclude dead cells. Cells with CD41-GFP^{low} positive signal were
639 subjected to fluorescence-activated cell sorting (FACS) with an influx cytometer (BD
640 Biosciences, San Jose, CA, USA). Single-cell RNA sequencing was performed
641 according to an adapted version of the SORT-seq (Muraro et al., 2016) with adapted
642 primers described in (Van Den Brink et al., 2017). In short, single cells were FACS

643 sorted, as described above, on 384-well plates containing 384 primers and Mineral
644 oil (Sigma Aldrich). After sorting, plates were snap-frozen on dry ice and stored at -
645 80°C. For amplification cells were heat-lysed at 65°C followed by cDNA synthesis
646 using the CEL-seq2 (Hashimshony et al., 2016) and robotic liquid handling platforms.
647 After the second strand cDNA synthesis, the barcoded material was pooled into
648 libraries of 384 cells and amplified using *in vitro* transcription. Following amplification,
649 the rest of the CEL-seq2 protocol was followed for preparation of the amplified cDNA
650 library, using TruSeq small RNA primers (Illumina, San Diego, CA, USA). The DNA
651 library was paired-end sequenced on an Illumina Nextseq™ 500 (Illumina), high
652 output, with a 1x75 bp Illumina kit (R1:26 cycles, index read: 6 cycles, R2:60 cycles).
653 **Data analysis of single-cell RNA sequencing**
654 During sequencing, Read1 was assigned 26 base pairs and was used for
655 identification of the Ilumina library barcode, cell barcode and unique molecular
656 identifier. Read2 was assigned 60 base pairs and used to map to the reference
657 transcriptome of Zv9 Danio rerio. Data was demultiplexed as described in (Grün et
658 al., 2014). Single cell transcriptomics analysis was done using the RaceID3
659 algorithm (Herman et al., 2018), following an adapted version of the RaceID manual
660 (https://cran.r-project.org/web/packages/RaceID/vignettes/RaceID.html) using R-
661 3.5.2. In total 768 cells per genotype were sequenced for the datasets. After
662 removing cells with less than 1000 UMIs and only keeping genes that were detected
663 with at least 3 UMIs in 1 cell, 439 wt, 384 D61G/wt and 543 D61G/D61G cells were
664 left for further analysis. Batch effects observed for plates which were prepared on
665 different days was removed using the scran function. 4 major clusters and 5 minor
666 clusters were identified. The minor clusters contained 130 cells in total and were
667 excluded from further analysis for statistical reasons. Differential gene expression
668 analysis was done as described in (Muraro et al., 2016) with an adapted version of
669 the DESseq2 (Love et al., 2014). GO term enrichment analysis for differentially
670 expressed genes of each major cluster was performed using the DAVID
671 Bioinformatics Resources 6.8 (https://david.ncifcrf.gov/). Trajectory inference and
672 pseudotime analysis were done using Monocle3 (v1.0.0). The data was subset to
673 include the major cell types; HSC-like cells, thrombocyte and erythrocyte
674 progenitors, early myeloid progenitors, and monocyte/macrophage progenitors. The
675 normalized counts, tSNE coordinates and clusters generated by RaceID3 were used
676 for trajectory inference. To investigate the potential lineage differentiation path, the

677 HSC-like cluster (center) was then selected as root for pseudotime analysis and
678 used to order cells in pseudotime.

679

680 **RNA sequencing and differential gene expression analysis of the patient**
681 **material**

682 Libraries were prepared with TruSeq® Stranded Total RNASample preparation kit
683 (Illumina) according to supplier's recommendations. Briefly, the ribosomal RNA
684 fraction was removed from 1µg of total RNA using the Ribo-Zero™ Gold Kit (Illumina).
685 Fragmentation was then achieved using divalent cations under elevated temperature
686 to obtain approximately 300bp pieces. Double strand cDNA synthesis was performed
687 using reverse transcriptase and random primers, Illumina adapters were ligated and
688 cDNA library was PCR amplified for sequencing. Paired-end 75b sequencing was then
689 carried out on a HiSeq4000 (Illumina). Quality of reads was assessed for each sample
690 using FastQC (http://www.bioinformatics.babraham.ac.uk/projects/fastqc/). A subset
691 of 500,000 reads from each Fastq file was aligned to the reference human genome
692 hg19/GRCh37 with tophat2 to determine insert sizes with Picard. Full Fastq files were
693 aligned to the reference human genome hg19/GRCh37 with tophat2 (-p 24 -r 150 -g 2
694 --library-type fr-firststrand) (Kim et al., 2013). We removed reads mapping to multiple
695 locations. STAR was used to obtain the number of reads associated with each gene
696 in the Gencode v26lift37 annotation (restricted to protein-coding genes, antisense, and
697 lincRNAs). Raw counts for each sample were imported into R statistical software using
698 the Bioconductor DESeq2 package. Extracted count matrix was normalized for library
699 size and coding length of genes to compute TPM expression levels. Differential gene
700 expression analysis was performed using the Bioconductor limma package and the
701 voom transformation. To improve the statistical power of the analysis, only genes
702 expressed in at least one sample (TPM >0.3) were considered. A qval threshold of <
703 0.05 and a minimum fold change of 1.2 were used to define differentially expressed
704 genes. Due to the imbalance between male and female samples, sex differences were
705 adjusted with the function model.matrix from the stats package. RNAseq data analysis
706 was performed with Galileo® v1.4.4, an interactive R shiny application.
707 Representations of the gene expression levels were performed with the library ggplot2
708 and R 4.0.2.

709 **Pathway enrichment analysis (GSEA) and Principal component analysis (PCA)**

710 Gene set enrichment analysis was performed by clusterProfiler::GSEA function using
711 the fgsea algorithm. Gene list from the differential analysis was ordered by decreasing
712 log2 (fold change). Hallmark classes Gene sets from the MSigDB v7.2 database were
713 selected keeping only gene sets defined by 10-500 genes. The p-values were adjusted
714 by the Benjamini-Hochberg (FDR) procedure. The custom zebrafish signature was
715 built from the human orthologous genes of the 100 most overexpressed zebrafish
716 genes based on the log2 (Fold Change) derived from the monocyte/macrophage
717 progenitor cluster of the zebrafish HSPCs single cell sequencing dataset. The
718 Bioconductor edgeR package was used to import raw counts into R, and compute
719 normalized log2 CPM (counts per millions of mapped reads) using the TMM (weighted
720 trimmed mean of M-values) as normalization procedure. The normalized expression
721 matrix from the 100 most overexpressed genes (based on log2FC in the zebrafish
722 dataset) was used to classify the samples according to their gene expression patterns
723 using principal component analysis (PCA). PCA was performed by FactoMineR::PCA
724 function with “ncp = 10, scale.unit = FALSE” parameters.

725 **Statistical analysis**

726 Data was plotted in GraphPad Prism 7.05 (GraphPad Software Inc., San Diego, CA,
727 USA), except for the violin plots of gene expression, which were plotted in R using
728 ggplot2(Wickham, 2009). Statistical difference analysis was performed using the
729 one-way ANOVA supplemented by Tukey’s HSD test in GraphPad Prism 7.05,
730 except for the gene expression differences in single cell RNA sequencing data,
731 where T-test was performed in Rstudio 1.1.463 (Rstudio, Boston, MA, USA), and the
732 treatment WISH experiments, where Chi-squared test was performed in GraphPad
733 Prism 7.05. Significant difference was considered when $p<0.05$ (*$p<0.05$, **$p<0.01$,
734 ***$p<0.001$, NS=non significant).

Author Contributions

MS Conceptualization, Methodology, Formal analysis, Investigation, Data Curation, Writing - Original Draft, Visualization, **SBF** Investigation, Formal analysis, Data Curation, Methodology, Writing - Review & Editing, **FP** Investigation, Formal Analysis, Methodology, Writing - Review Editing, **CY, QY** Investigation- performed transplantation experiments, Data Curation, Formal analysis, Methodology, Writing - Review & Editing**, MS** Investigation, Formal Analysis, Methodology**, SMK** Investigation- provided assistance with heart function analysis, Methodology, Resources, Writing - Review & Editing**, PA** Investigation, Formal analysis, **JB** Conceptualization, Supervision, Writing - Review & Editing**, DML** Conceptualization, Supervision, Writing - Review & Editing**, HC** Conceptualization, Supervision, Writing - Review & Editing, **JDH** Conceptualization, Supervision, Funding acquisition, Project administration, Writing - Original Draft

Acknowledgements

We thank the laboratory of Niels Geijsen (Hubrecht Institute) for providing us with Cas9 protein, Petr Bartunek and Olga Machanova (Institute of Molecular Genetics, Academy of Sciences of the Czech Republic v.v.i. Prague) and Geert Wiegertjes (University Wageningen) for cytokines and carp serum, Stefan van der Elst for assistance with FACS sorting, Hubrecht Institute animal caretakers for animal support and Single Cell Discoveries and Chloé Baron for support with single cell RNA sequencing. This work was supported by E-Rare grant NSEuroNet (JdH and HC), EJPRD grant NSEuroNet (JdH and HC), NIH grants R01CA211734 (D.M.L) and R24OD016761 (D.M.L), the MGH Research Scholar Award (D.M.L.) and Alex Lemonade Stand Foundation (C.Y.).

759 # Competing Interests:

760 The authors declare no competing interests.

References

Aleström, P., D'Angelo, L., Midtlyng, P. J., Schorderet, D. F., Schulte-Merker, S., Sohm, F., & Warner, S. (2020). Zebrafish: Housing and husbandry recommendations. *Laboratory Animals*, *54*(3), 213–224. https://doi.org/10.1177/0023677219869037

Araki, T., Chan, G., Newbigging, S., Morikawa, L., Bronson, R., & Neel, B. G. (2009). Noonan syndrome cardiac defects are caused by PTPN11 acting in endocardium to enhance endocardial-mesenchymal transformation. *Proceedings of the National Academy of Sciences of the United States of America*, *106*(12), 4736–4741. https://doi.org/10.1073/pnas.0810053106

Araki, T., Mohi, M. G., Ismat, F. A., Bronson, R. T., Williams, I. R., Kutok, J. L., Yang, W., Pao, L. I., Gilliland, D. G., Epstein, J. A., & Neel, B. G. (2004). Mouse model of Noonan syndrome reveals cell type- and gene dosage-dependent effects of Ptpn11 mutation. *Nature Medicine*, *10*(8), 849–857. https://doi.org/10.1038/nm1084

Arranz, L., Arriero, M. del M., & Villatoro, A. (2017). Interleukin-1β as emerging therapeutic target in hematological malignancies and potentially in their complications. In *Blood Reviews* (Vol. 31, Issue 5, pp. 306–317). Churchill Livingstone. https://doi.org/10.1016/j.blre.2017.05.001

Bagby, G. C., Dinarello, C. A., Neerhout, R. C., Ridgway, D., & McCall, E. (1988). Interleukin 1-dependent paracrine granulopoiesis in chronic granulocytic leukemia of the juvenile type. *Journal of Clinical Investigation*, *82*(4), 1430–1436. https://doi.org/10.1172/JCI113748

Behnert, A., Meyer, J., Parsa, J.-Y., Hechmer, A., Loh, M. L., Olshen, A., Smith, A. J. de, & Stieglitz, E. (2021). Exploring the genetic and epigenetic origins of juvenile

786 myelomonocytic leukemia using newborn screening samples. *Leukemia 2021*,
787 1–4. https://doi.org/10.1038/s41375-021-01331-0
788 Bonetti, M., Rodriguez-Martinez, V., Overman, J. P., Overvoorde, J., Van Eekelen,
789 M., Jopling, C., & Den Hertog, J. (2014). Distinct and overlapping functions of
790 ptpn11 genes in zebrafish development. *PLoS ONE*, *9*(4), e94884.
791 https://doi.org/10.1371/journal.pone.0094884
792 Caye, A., Rouault-Pierre, K., Strullu, M., Lainey, E., Abarrategi, A., Fenneteau, O.,
793 Arfeuille, C., Osman, J., Cassinat, B., Pereira, S., Anjos-Afonso, F., Currie, E.,
794 Ariza-McNaughton, L., Barlogis, V., Dalle, J. H., Baruchel, A., Chomienne, C.,
795 Cavé, H., & Bonnet, D. (2019). Despite mutation acquisition in hematopoietic
796 stem cells, JMML-propagating cells are not always restricted to this
797 compartment. *Leukemia*, 1–11. https://doi.org/10.1038/s41375-019-0662-y
798 Caye, A., Strullu, M., Guidez, F., Cassinat, B., Gazal, S., Fenneteau, O., Lainey, E.,
799 Nouri, K., Nakhaei-Rad, S., Dvorsky, R., Lachenaud, J., Pereira, S., Vivent, J.,
800 Verger, E., Vidaud, D., Galambrun, C., Picard, C., Petit, A., Contet, A., … Cavé,
801 H. (2015). Juvenile myelomonocytic leukemia displays mutations in components
802 of the RAS pathway and the PRC2 network. *Nature Genetics 2015 47:11*,
803 *47*(11), 1334–1340. https://doi.org/10.1038/ng.3420
804 Chan, G., Kalaitzidis, D., Usenko, T., Kutok, J. L., Yang, W., Mohi, M. G., & Neel, B.
805 G. (2009). Leukemogenic Ptpn11 causes fatal myeloproliferative disorder via
806 cell-autonomous effects on multiple stages of hematopoiesis. *Blood*, *113*(18),
807 4414–4424. https://doi.org/10.1182/BLOOD-2008-10-182626
808 Choorapoikayil, S., Kers, R., Herbomel, P., Kissa, K., & den Hertog, J. (2014).
809 Pivotal role of Pten in the balance between proliferation and differentiation of
810 hematopoietic stem cells in zebrafish. *Blood*, *123*(2), 184–190.

811 https://doi.org/10.1182/BLOOD-2013-05-501544
812 Choorapoikayil, S., Kuiper, R. V, de Bruin, A., & den Hertog, J. (2012).
813 Haploinsufficiency of the genes encoding the tumor suppressor Pten
814 predisposes zebrafish to hemangiosarcoma. *Disease Models & Mechanisms*,
815 *5*(2), 241–247. https://doi.org/10.1242/dmm.008326
816 Craver, B. M., El Alaoui, K., Scherber, R. M., & Fleischman, A. G. (2018). The critical
817 role of inflammation in the pathogenesis and progression of myeloid
818 malignancies. In *Cancers* (Vol. 10, Issue 4). MDPI AG.
819 https://doi.org/10.3390/cancers10040104
820 de Pater, E., & Trompouki, E. (2018). Bloody Zebrafish: Novel Methods in Normal
821 and Malignant Hematopoiesis. *Frontiers in Cell and Developmental Biology*, *6*,
822 124. https://doi.org/10.3389/fcell.2018.00124
823 Dong, L., Yu, W. M., Zheng, H., Loh, M. L., Bunting, S. T., Pauly, M., Huang, G.,
824 Zhou, M., Broxmeyer, H. E., Scadden, D. T., & Qu, C. K. (2016).
825 Leukaemogenic effects of Ptpn11 activating mutations in the stem cell
826 microenvironment. *Nature*, *539*(7628), 304–308.
827 https://doi.org/10.1038/nature20131
828 Ehrchen, J. M., Roth, J., & Barczyk-Kahlert, K. (2019). More Than Suppression:
829 Glucocorticoid Action on Monocytes and Macrophages. *Frontiers in*
830 *Immunology*, *0*(AUG), 2028. https://doi.org/10.3389/FIMMU.2019.02028
831 Ellett, F., Pase, L., Hayman, J. W., Andrianopoulos, A., & Lieschke, G. J. (2011).
832 mpeg1 promoter transgenes direct macrophage-lineage expression in zebrafish.
833 *Blood*, *117*(4), e49. https://doi.org/10.1182/blood-2010-10-314120
834 Freedman, M. H., Cohen, A., Grunberger, T., Bunin, N., Luddy, R. E., Saunders, E.
835 F., Shahidi, N., Lau, A., & Estrov, Z. (1992). Central role of tumour necrosis

836 factor, GM-CSF, and interleukin 1 in the pathogenesis of juvenile chronic
837 myelogenous leukaemia. *British Journal of Haematology*, *80*(1), 40–48.
838 https://doi.org/10.1111/j.1365-2141.1992.tb06398.x
839 Gagnon, J. A., Valen, E., Thyme, S. B., Huang, P., Akhmetova, L., Ahkmetova, L.,
840 Pauli, A., Montague, T. G., Zimmerman, S., Richter, C., & Schier, A. F. (2014).
841 Efficient mutagenesis by Cas9 protein-mediated oligonucleotide insertion and
842 large-scale assessment of single-guide RNAs. *PloS One*, *9*(5), e98186.
843 https://doi.org/10.1371/journal.pone.0098186
844 Gore, A. V., Pillay, L. M., Venero Galanternik, M., & Weinstein, B. M. (2018). The
845 zebrafish: A fintastic model for hematopoietic development and disease. *Wiley*
846 *Interdisciplinary Reviews: Developmental Biology*, *7*(3), e312.
847 https://doi.org/10.1002/wdev.312
848 Grün, D., Kester, L., & Van Oudenaarden, A. (2014). Validation of noise models for
849 single-cell transcriptomics. *Nature Methods*, *11*(6), 637–640.
850 https://doi.org/10.1038/nmeth.2930
851 Hale, A. J., & den Hertog, J. (2017). Shp2–Mitogen-Activated Protein Kinase
852 Signaling Drives Proliferation during Zebrafish Embryo Caudal Fin Fold
853 Regeneration. *Molecular and Cellular Biology*, *38*(4).
854 https://doi.org/10.1128/mcb.00515-17
855 Hashimshony, T., Senderovich, N., Avital, G., Klochendler, A., de Leeuw, Y., Anavy,
856 L., Gennert, D., Li, S., Livak, K. J., Rozenblatt-Rosen, O., Dor, Y., Regev, A., &
857 Yanai, I. (2016). CEL-Seq2: Sensitive highly-multiplexed single-cell RNA-Seq.
858 *Genome Biology*, *17*(1), 77. https://doi.org/10.1186/s13059-016-0938-8
859 Herman, J. S., Sagar, & Grün, D. (2018). FateID infers cell fate bias in multipotent
860 progenitors from single-cell RNA-seq data. *Nature Methods*, *15*(5), 379–386.

861 https://doi.org/10.1038/nmeth.4662
862 Hogan, B. M., Bos, F. L., Bussmann, J., Witte, M., Chi, N. C., Duckers, H. J., &
863 Schulte-Merker, S. (2009). Ccbe1 is required for embryonic lymphangiogenesis
864 and venous sprouting. *Nature Genetics*, *41*(4), 396–398.
865 https://doi.org/10.1038/ng.321
866 Hu, B., Zhang, W., Feng, X., Ji, W., Xie, X., & Xiao, W. (2014). Zebrafish eaf1
867 suppresses foxo3b expression to modulate transcriptional activity of gata1 and
868 spi1 in primitive hematopoiesis. *Developmental Biology*, *388*(1), 81–93.
869 https://doi.org/10.1016/j.ydbio.2014.01.005
870 Jopling, C., Van Geemen, D., & Den Hertog, J. (2007). Shp2 knockdown and
871 noonan/LEOPARD mutant Shp2-induced gastrulation defects. *PLoS Genetics*,
872 *3*(12), e225. https://doi.org/10.1371/journal.pgen.0030225
873 Kratz, C. P., Niemeyer, C. M., Castleberry, R. P., Cetin, M., Bergsträsser, E.,
874 Emanuel, P. D., Hasle, H., Kardos, G., Klein, C., Kojima, S., Stary, J., Trebo, M.,
875 Zecca, M., Gelb, B. D., Tartaglia, M., & Loh, M. L. (2005). The mutational
876 spectrum of PTPN11 in juvenile myelomonocytic leukemia and Noonan
877 syndrome/myeloproliferative disease. *Blood*, *106*(6), 2183–2185.
878 https://doi.org/10.1182/blood-2005-02-0531
879 Lin, H. F., Traver, D., Zhu, H., Dooley, K., Paw, B. H., Zon, L. I., & Handin, R. I.
880 (2005). Analysis of thrombocyte development in CD41-GFP transgenic
881 zebrafish. *Blood*, *106*(12), 3803–3810. https://doi.org/10.1182/blood-2005-01-
882 0179
883 Louka, E., Povinelli, B., Rodriguez-Meira, A., Buck, G., Wen, W. X., Wang, G.,
884 Sousos, N., Ashley, N., Hamblin, A., Booth, C. A. G., Roy, A., Elliott, N.,
885 Iskander, D., De La Fuente, J., Fordham, N., O'Byrne, S., Inglott, S., Norfo, R.,

886 Salio, M., … Mead, A. J. (2021). Heterogeneous disease-propagating stem cells
887 in juvenile myelomonocytic leukemia. *Journal of Experimental Medicine*, *218*(2).
888 https://doi.org/10.1084/JEM.20180853
889 Love, M. I., Huber, W., & Anders, S. (2014). Moderated estimation of fold change
890 and dispersion for RNA-seq data with DESeq2. *Genome Biology*, *15*(12), 550.
891 https://doi.org/10.1186/s13059-014-0550-8
892 Moore, J. C., Tang, Q., Yordán, N. T., Moore, F. E., Garcia, E. G., Lobbardi, R.,
893 Ramakrishnan, A., Marvin, D. L., Anselmo, A., Sadreyev, R. I., & Langenau, D.
894 M. (2016). Single-cell imaging of normal and malignant cell engraftment into
895 optically clear prkdc-null scid zebrafish. *Journal of Experimental Medicine*,
896 *213*(12), 2575–2589. https://doi.org/10.1084/jem.20160378
897 Mulero-Navarro, S., Sevilla, A., Roman, A. C., Lee, D.-F., D'Souza, S. L., Pardo, S.,
898 Riess, I., Su, J., Cohen, N., Schaniel, C., Rodriguez, N. A., Baccarini, A., Brown,
899 B. D., Cavé, H., Caye, A., Strullu, M., Yalcin, S., Park, C. Y., Dhandapany, P. S.,
900 … Gelb, B. D. (2015). Myeloid Dysregulation in a Human Induced Pluripotent
901 Stem Cell Model of PTPN11 -Associated Juvenile Myelomonocytic Leukemia.
902 *Cell Reports*, *13*(3), 504–515. https://doi.org/10.1016/j.celrep.2015.09.019
903 Muraro, M. J., Dharmadhikari, G., Grün, D., Groen, N., Dielen, T., Jansen, E., van
904 Gurp, L., Engelse, M. A., Carlotti, F., de Koning, E. J. P., & van Oudenaarden,
905 A. (2016). A Single-Cell Transcriptome Atlas of the Human Pancreas. *Cell*
906 *Systems*, *3*(4), 385-394.e3. https://doi.org/10.1016/j.cels.2016.09.002
907 Niihori, T., Nagai, K., Fujita, A., Ohashi, H., Okamoto, N., Okada, S., Harada, A.,
908 Kihara, H., Arbogast, T., Funayama, R., Shirota, M., Nakayama, K., Abe, T.,
909 Inoue, S. ichi, Tsai, I. C., Matsumoto, N., Davis, E. E., Katsanis, N., & Aoki, Y.
910 (2019). Germline-Activating RRAS2 Mutations Cause Noonan Syndrome.

American Journal of Human Genetics, *104*(6), 1233–1240. https://doi.org/10.1016/j.ajhg.2019.04.014

Ogryzko, N. V., Lewis, A., Wilson, H. L., Meijer, A. H., Renshaw, S. A., & Elks, P. M. (2019). Hif-1α–Induced Expression of Il-1β Protects against Mycobacterial Infection in Zebrafish. *The Journal of Immunology*, *202*(2), 494–502. https://doi.org/10.4049/JIMMUNOL.1801139

Oltova, J., Svoboda, O., & Bartunek, P. (2018). Hematopoietic Cytokine Gene Duplication in Zebrafish Erythroid and Myeloid Lineages. *Frontiers in Cell and Developmental Biology*, *6*(DEC), 174. https://doi.org/10.3389/FCELL.2018.00174

Paardekooper Overman, J., Yi, J.-S., Bonetti, M., Soulsby, M., Preisinger, C., Stokes, M. P., Hui, L., Silva, J. C., Overvoorde, J., Giansanti, P., Heck, A. J. R., Kontaridis, M. I., Den Hertog, J., & Bennett, A. M. (2014). PZR Coordinates Shp2 Noonan and LEOPARD Syndrome Signaling in Zebrafish and Mice. *Molecular and Cellular Biology*, *34*(15), 2874–2889. https://doi.org/10.1128/MCB.00135-14

Rauen, K. A. (2013). The RASopathies. *Annu. Rev. Genomics Hum. Genet*, *14*, 355–369. https://doi.org/10.1146/annurev-genom-091212-153523

Renshaw, S. A., Loynes, C. A., Trushell, D. M. I., Elworthy, S., Ingham, P. W., & Whyte, M. K. B. (2006). A transgenic zebrafish model of neutrophilic inflammation. *Blood*, *108*(13), 3976–3978. https://doi.org/10.1182/blood-2006-05-024075

Runtuwene, V., van Eekelen, M., Overvoorde, J., Rehmann, H., Yntema, H. G., Nillesen, W. M., van Haeringen, A., van der Burgt, I., Burgering, B., & den Hertog, J. (2011). Noonan syndrome gain-of-function mutations in NRAS cause zebrafish gastrulation defects. *Disease Models & Mechanisms*, *4*(3), 393–399.

https://doi.org/10.1242/dmm.007112

Stachura, D. L., Svoboda, O., Campbell, C. A., Espín-Palazón, R., Lau, R. P., Zon, L. I., Bartůněk, P., & Traver, D. (2013). The zebrafish granulocyte colony-stimulating factors (Gcsfs): 2 paralogous cytokines and their roles in hematopoietic development and maintenance. *Blood*, *122*(24), 3918. https://doi.org/10.1182/BLOOD-2012-12-475392

Strullu, M., Caye, A., Lachenaud, J., Cassinat, B., Gazal, S., Fenneteau, O., Pouvreau, N., Pereira, S., Baumann, C., Contet, A., Sirvent, N., Méchinaud, F., Guellec, I., Adjaoud, D., Paillard, C., Alberti, C., Zenker, M., Chomienne, C., Bertrand, Y., … Cavé, H. (2014). Juvenile myelomonocytic leukaemia and Noonan syndrome. *Journal of Medical Genetics*, *51*(10), 689–697. https://doi.org/10.1136/jmedgenet-2014-102611

Svoboda, O., Stachura, D. L., MacHonova, O., Zon, L. I., Traver, D., & Bartunek, P. (2016). Ex vivo tools for the clonal analysis of zebrafish hematopoiesis. *Nature Protocols*, *11*(5), 1007–1020. https://doi.org/10.1038/nprot.2016.053

Tajan, M., de Rocca Serra, A., Valet, P., Edouard, T., & Yart, A. (2015). SHP2 sails from physiology to pathology. In *European Journal of Medical Genetics* (Vol. 58, Issue 10, pp. 509–525). https://doi.org/10.1016/j.ejmg.2015.08.005

Tajan, M., Paccoud, R., Branka, S., Edouard, T., & Yart, A. (2018). The RASopathy Family: Consequences of Germline Activation of the RAS/MAPK Pathway. *Endocrine Reviews*, *39*(5), 676–700. https://doi.org/10.1210/er.2017-00232

Tang, Q., Abdelfattah, N. S., Blackburn, J. S., Moore, J. C., Martinez, S. A., Moore, F. E., Lobbardi, R., Tenente, I. M., Ignatius, M. S., Berman, J. N., Liwski, R. S., Houvras, Y., & Langenau, D. M. (2014). Optimized cell transplantation using adult rag2 mutant zebrafsh. *Nature Methods*, *11*(8), 821–824. https://doi.org/10.1038/nmeth.3031

Tarnawsky, S. P., Yoshimoto, M., Deng, L., Chan, R. J., & Yoder, M. C. (2017). Yolk

964 Sac Erythromyeloid Progenitors Expressing Gain Of Function PTPN11 Have
965 Functional Features Of JMML But Are Not Sufficient To Cause Disease In Mice.
966 *Developmental Dynamics : An Official Publication of the American Association of*
967 *Anatomists*, *246*(12), 1001. https://doi.org/10.1002/DVDY.24598
968 Tarnawsky, S. P., Yu, W.-M., Qu, C.-K., Chan, R. J., & Yoder, M. C. (2018).
969 Hematopoietic-restricted Ptpn11E76K reveals indolent MPN progression in
970 mice. *Oncotarget*, *9*(31), 21831. https://doi.org/10.18632/ONCOTARGET.25073
971 Tartaglia, M., Mehler, E. L., Goldberg, R., Zampino, G., Brunner, H. G., Kremer, H.,
972 Van der Burgt, I., Crosby, A. H., Ion, A., Jeffery, S., Kalidas, K., Patton, M. A.,
973 Kucherlapati, R. S., & Gelb, B. D. (2001). Mutations in PTPN11, encoding the
974 protein tyrosine phosphatase SHP-2, cause Noonan syndrome. *Nature*
975 *Genetics*, *29*(4), 465–468. https://doi.org/10.1038/ng772
976 Tartaglia, M., Niemeyer, C. M., Fragale, A., Song, X., Buechner, J., Jung, A., Hählen,
977 K., Hasle, H., Licht, J. D., & Gelb, B. D. (2003). Somatic mutations in PTPN11 in
978 juvenile myelomonocytic leukemia, myelodysplastic syndromes and acute
979 myeloid leukemia. *Nature Genetics*, *34*(2), 148–150.
980 https://doi.org/10.1038/ng1156
981 Tessadori, F., Roessler, H. I., Savelberg, S. M. C., Chocron, S., Kamel, S. M.,
982 Duran, K. J., Van Haelst, M. M., Van Haaften, G., & Bakkers, J. (2018). Effective
983 CRISPR/Cas9-based nucleotide editing in zebrafish to model human genetic
984 cardiovascular disorders. *Disease Models and Mechanisms*, *11*(10).
985 https://doi.org/10.1242/dmm.035469
986 Tessadori, F., van Weerd, J. H., Burkhard, S. B., Verkerk, A. O., de Pater, E.,
987 Boukens, B. J., Vink, A., Christoffels, V. M., & Bakkers, J. (2012). Identification
988 and Functional Characterization of Cardiac Pacemaker Cells in Zebrafish. *PLoS*

989 *ONE*, *7*(10), e47644. https://doi.org/10.1371/journal.pone.0047644
990 Thisse, C., Thisse, B., Schilling, T. F., & Postlethwait, J. H. (1993). Structure of the
991 zebrafish snail1 gene and its expression in wild-type, spadetail and no tail
992 mutant embryos. *Development*, *119*(4).
993 Van Den Brink, S. C., Sage, F., Vértesy, Á., Spanjaard, B., Peterson-Maduro, J.,
994 Baron, C. S., Robin, C., & Van Oudenaarden, A. (2017). Single-cell sequencing
995 reveals dissociation-induced gene expression in tissue subpopulations. In
996 *Nature Methods* (Vol. 14, Issue 10, pp. 935–936). Nature Publishing Group.
997 https://doi.org/10.1038/nmeth.4437
998 Westerfield, M. (2000). *The Zebrafish Book: A Guide for the Laboratory Use of*
999 *Zebrafish (Danio Rerio)* (4th ed.). University of Oregon Press.
1000 Wickham, H. (2009). *ggplot2: Elegant Graphics for Data Analysis*. Springer
1001 International Publishing. https://ggplot2.tidyverse.org.
1002 Xie, Y., Meijer, A. H., & Schaaf, M. J. M. (2021). Modeling Inflammation in Zebrafish
1003 for the Development of Anti-inflammatory Drugs. *Frontiers in Cell and*
1004 *Developmental Biology*, *8*. https://doi.org/10.3389/FCELL.2020.620984
1005 Xu, D., Liu, X., Yu, W. M., Meyerson, H. J., Guo, C., Gerson, S. L., & Qu, C. K.
1006 (2011). Non-lineage/stage-restricted effects of a gain-of-function mutation in
1007 tyrosine phosphatase Ptpn11 (Shp2) on malignant transformation of
1008 hematopoietic cells. *Journal of Experimental Medicine*, *208*(10), 1977–1988.
1009 https://doi.org/10.1084/jem.20110450
1010